

Supporting Information

Hydrogen-bond-regulated Hierarchical Porous Organic Polymers for Enhanced Photocatalytic H₂O₂ Production

*Xiaojuan Bai, ^{*a,b} Rujiao Liu,^b Aofei Wang,^b Linlong Guo,^b Ruilong Zong^c and Zhen Wei ^{*d}*

^aKey Laboratory of Urban Stormwater System and Water Environment, Ministry of Education, Beijing University of Civil Engineering and Architecture, Beijing 100044, China.

^bBeijing Energy Conservation & Sustainable Urban and Rural Development Provincial and Ministry Co-construction Collaboration Innovation Center, Beijing University of Civil Engineering and Architecture, Beijing, China.

^cDepartment of Chemistry, Tsinghua University, Beijing 100084, China.

^dBeijing Key Laboratory for Green Catalysis and Separation, Key Laboratory of Beijing on Regional Air Pollution Control, Key Laboratory of Advanced Functional Materials, Education Ministry of China, Beijing University of Technology, Beijing 100124, China.

E-mail: baixiaojuan@bucea.edu.cn, heixia.1986@163.com (Xiaojuan Bai),
xfwz522@126.com (Zhen Wei).

S1. Experimental Details	3
S2. Supplementary Figures	8
S3. Supplementary Tables.....	52
S4. Supplementary References.....	61

S1. Experimental Details

Characterization

The scanning electron microscopy (SEM) image was captured at Hitachi Ultra High Resolution Field Emission Scanning Electron Microscope SU8000, Japan. The HT7700 transmission electron microscope (TEM) (Hitachi, Japan) was used to characterize the morphology and structure of the material under an acceleration voltage of 100 kV. X-ray diffraction (XRD) patterns were obtained on a PHI 5300 ESCA diffractometer with Cu K α irradiation ($\lambda = 1.54 \text{ \AA}$). Fourier transform infrared spectroscopy (FTIR) spectra were recorded on a Bruker VERTEX 700 spectrometer. ^{13}C cross-polarization magic angle spinning (CP-MAS) solid-state nuclear magnetic resonance (NMR) spectra were recorded on a JNM-ECZ600R solid-state NMR spectrometer with a 3.2 mm magic-angle spinning probe. X-ray photoelectron spectroscopy (XPS) was measured on a Al Alpha XPS instrument ESCALAB Xi+ (Thermo Fisher Scientific, USA). The thermal gravimetric analysis (TGA) was measured on a Mettler Toledo with a range of 30–800 °C. BET specific surface area was determined by nitrogen adsorption–desorption isotherm measured at 77 K (Micromeritics APSP2460, USA). The room temperature photoluminescence (PL) spectra of materials were recorded on PerkinElmer LS55 spectrophotometer. Fluorescence lifetimes were tested by the Edinburgh FLS1000 (UK). The steady-state surface photovoltage (SPV) was tested on a CEL-SPS1000. UV–vis diffuse reflectance spectra were recorded on a UV-2600 spectrometer (Techcomp, China). Photoluminescence spectra were recorded using a PerkinElmer LS55 spectrofluorometer. Electron paramagnetic resonance (EPR) spectra were measured at room temperature using ESR 300E (Bruker, Germany) spectrometer. The electrochemical impedance and photocurrent response were performed by the CHI-660E electrochemical workstations (CH Instruments, China) with 0.1 M Na $_2$ SO $_4$ aqueous solution. Hall effect was tested on Ecopia HMS-7000.

Photocatalytic H $_2$ O $_2$ production

5 mg of photocatalyst was added to 25 ml of deionized water, and oxygen adsorption equilibrium was achieved by stirring for 30 min in the dark. Then, 1.5 ml of the suspension was removed every 30 min under visible light irradiation, the filtered solution was centrifuged. The amount of H $_2$ O $_2$ was analyzed by iodometry. 0.5 mL of 0.1 mol L $^{-1}$ potassium hydrogen phthalate (C $_8$ H $_5$ KO $_4$) aqueous solution and 0.5 mL of 0.4 mol L $^{-1}$ potassium iodide (KI) aqueous solution were added to the obtained solution, which was then kept for 30 min. The H $_2$ O $_2$ molecules reacted with iodide anions (I $^-$) under acidic conditions (H $_2$ O $_2 + 3\text{I}^- + 2\text{H}^+ \rightarrow \text{I}^{3-} + 2\text{H}_2\text{O}$) to produce triiodide anions.

The amount of H $_2$ O $_2$ was determined using UV–vis spectroscopy based on the absorbance at 350 nm. The apparent quantum yields (AQY) for H $_2$ O $_2$ production were measured under monochromatic light produced from a 300 W Xe lamp with band-pass filter. The AQY values are calculated by the following equation:

$$\text{AQY} = \frac{N_{\text{H}_2\text{O}_2}}{N_p} = \frac{2N_a \times M_{\text{H}_2\text{O}_2} \times hc}{\text{PSt}\lambda} \times 100\%$$

Where M corresponds to the amount of produced H₂O₂ (mol); Na and h represent the Avogadro constant (6.022×10²³/mol) and Planck constant (6.626×10⁻³⁴ J·S); c is the light velocity (3×10⁸ m/s); S is the irradiation area (19.6 cm² in this work); P is the intensity of incident light (W/m²); t is attributed to the reaction time (3600 s in this work); λ represents the wavelength of the incident monochromatic light (m). In this experiment, the light intensities at wavelengths of 380 nm, 420 nm, 450 nm, 500 nm, and 550 nm were 31.58, 81.51, 99.85, 128.37 and 120.22 W/m², respectively. The solar-to-chemical energy conversion (SCC) efficiency was determined by using an AM 1.5G solar simulator as the light source (100 mW cm⁻²). 300 mg of catalyst and 500 ml of pure water were used for the SCC test without continuous O₂ input during the photocatalytic test.

$$\text{SCC efficiency}(\%) = \frac{[\Delta G \text{ for H}_2\text{O}_2 \text{ Generation}(\text{J mol}^{-1})][\text{H}_2\text{O}_2 \text{ formed}(\text{mol})]}{[\text{total input power}(\text{W})][\text{reaction time}(\text{s})]} \times 100\%$$

where ΔG= 117 kJ mol⁻¹. For example, when using Dha-TAPP as the catalyst, the irradiated sample areas are 16 cm² during 1 h of on sun illumination. Therefore, the calculated total input energy is 5760 J. During the 1 h photocatalytic reaction, x μmol H₂O₂ is generated and the energy generated by H₂O₂ formed is 0.117x J. SCC Efficiency=0.117x/5760.

The optical power was determined by a PLS-SXE300D Xe lamp (Beijing Perfect Light Technology Co., Ltd., Beijing, China).

Photocatalytic degradation of antibiotics

10 mg catalyst (Dha-TAPP) was added into 50 ml of 10 ppm antibiotics (CIP, SMX and DCF) solution in a 50 ml beaker and ultrasonically dispersed for 15 min in the dark. Before irradiation, the mixture was stirred in the dark for 30 min to reach the adsorption-desorption equilibrium. 1.5 ml of solution was taken out at stated intervals and centrifuged to remove the catalyst. The efficiency of the degradation of the antibiotics was measured by Acquity UPLC H-Class (Waters, America). The mobile phases of CIP and SMX consisted of MeOH and 0.1% formic acid solution (60: 40, v/v) with a flow rate of 0.3 ml/min and were used with a UV detector operating at 270 nm. The mobile phase of DCF consisted of methanol and 0.1% formic acid solution (70:30, v/v) at a flow rate of 0.2 ml/min using a UV detector with a wavelength of 278 nm.

Liquid Chromatography Mass Spectrometry measurement

The intermediates of photocatalytic degradation of CIP were determined using a liquid chromatography mass spectrometry system. The chromatographic separation was performed on a C18 column (5 μm, 250 mm × 3.5 mm) with an injection volume of 50 μL and a flow rate of 0.2 mL/min. The mobile phase composition was 40% methanol and 60% 0.1% formic acid aqueous solution. Mass spectral fragmentation data were collected using positive electrospray ionization (ESI+) mode with a scanning range of m/z 50 to 400.

Photocurrent measurement

The transient photocurrent response experiments were conducted on a CHI660E electrochemical system in a three-electrode system. The sample-coated Indium tin oxide (ITO) glass, Pt wire electrode, calomel electrode were used as the working electrode, counter electrode and the reference electrode, respectively. 0.1 M Na₂SO₄ solution was utilized as the electrolyte. E_{CB} (NHE, pH = 7) = E_{Fb} (SCE, pH = 7) - 0.2 + 0.24.

Rotating disk electrode (RDE) measurement

A glassy carbon rotating disk electrode (PINE Research Instrumentation, USA) served as the substrate for working electrode, and an Ag/AgCl electrode and a Pt wire electrode as the reference and counter electrode, respectively. The working electrode was prepared as followed: Pda-TAPP or Dha-TAPP (5 mg) were dispersed in EtOH (2 mL) containing Nafion (50 μ L) by ultrasonication. The slurry (20 μ L) was put onto the disk electrode and dried at room temperature. The linear sweep voltammograms (LSV) were obtained in an O₂-saturated 0.1 M phosphate buffer solution (pH = 7) at room temperature with a scan rate 10 mV s⁻¹ and different rotation speeds after O₂ bubbling for 10 min. During the reaction, light source from the Xe-lamp vertically illuminated at the rotating electrode, where the photoelectrochemical kinetic information and the formation of peroxide could be obtained. The average number of electrons (n) was calculated by Koutecky-Levich equation:

$$J^{-1} = J_k^{-1} + B^{-1} \omega^{-\frac{1}{2}}$$
$$B = 0.2nFv^{-\frac{1}{6}}CD^{\frac{2}{3}}$$

where J is the current density, J_k is the kinetic current density, ω is the rotating speed (rpm), F is the Faraday constant (96485 C mol⁻¹), ν is the kinetic viscosity of water (0.01 cm² s⁻¹), C is the bulk concentration of O₂ in water (1.26 \times 10⁻³ mol cm⁻³), and D is the diffusion coefficient of O₂ (2.7 \times 10⁻⁵ cm² s⁻¹), respectively.

O₂-Temperature Programmed Desorption (TPD) test

The O₂-TPD was tested on a Microtrac BELCat II (Japan). 50–100 mg of the sample was weighed and placed in a reaction tube. A controlled temperature ramp was initiated from ambient temperature to 120 °C at a rate of 10 °C/min for a drying pre-treatment. The sample was then subjected to a He flow (30-50 mL/min) for a duration of 1 hour. Subsequently, the system was cooled to 50 °C, followed by the introduction of a 10% O₂/He mixed gas at a flow rate of 30–50 mL/min until saturation was achieved. The flow was then switched back to pure He (30–50 mL/min) for an additional hour to eliminate weakly adsorbed O₂ from the surface. Finally, under a He atmosphere, the temperature was ramped to 300 °C at a rate of 10 °C/min for the desorption process. The evolved gases were detected using a Thermal Conductivity Detector (TCD).

In-situ Fourier transform infrared spectrometer (FT-IR) analysis

The in-situ FT-IR was tested on a Bruker INVENIO R FT-IR. The experiments were tested under continuous O₂ and H₂O vapor flow conditions. The light source was a 300 W Xe lamp light source without filters. Before turning on the light, the samples were now in dark conditions for 30 min to reach O₂ adsorption equilibrium, and the baseline was obtained before the samples started to adsorb. Tests were performed every 10 min after the light was turned on for a total of 60 min.

Computational Details

The density functional theory (DFT) calculations are carried out by using the DMol3 module in Materials Studio. The exchange-correlation interaction is described by generalized gradient approximation (GGA) with the Perdew–Burke–Ernzerhof (PBE) functional. The convergence tolerance is set as 10⁻⁵ Ha for energy and 0.002 Ha·Å⁻¹ for force. The Global orbital cutoff is set as

5.2 Å. The electron treatment was performed by double numerical plus d-functions (DNP) basis set. The adsorption energy (E_{ads}) of O_2 molecule on the surface is calculated as follow:

$$E_{\text{ads}} = E_{\text{total}} - E_{\text{surface}} - E_{\text{O}_2}$$

where E_{total} represents the energy of surface with adsorbed O_2 molecule, E_{surface} and E_{O_2} represent the energies of isolated surface and O_2 , respectively.

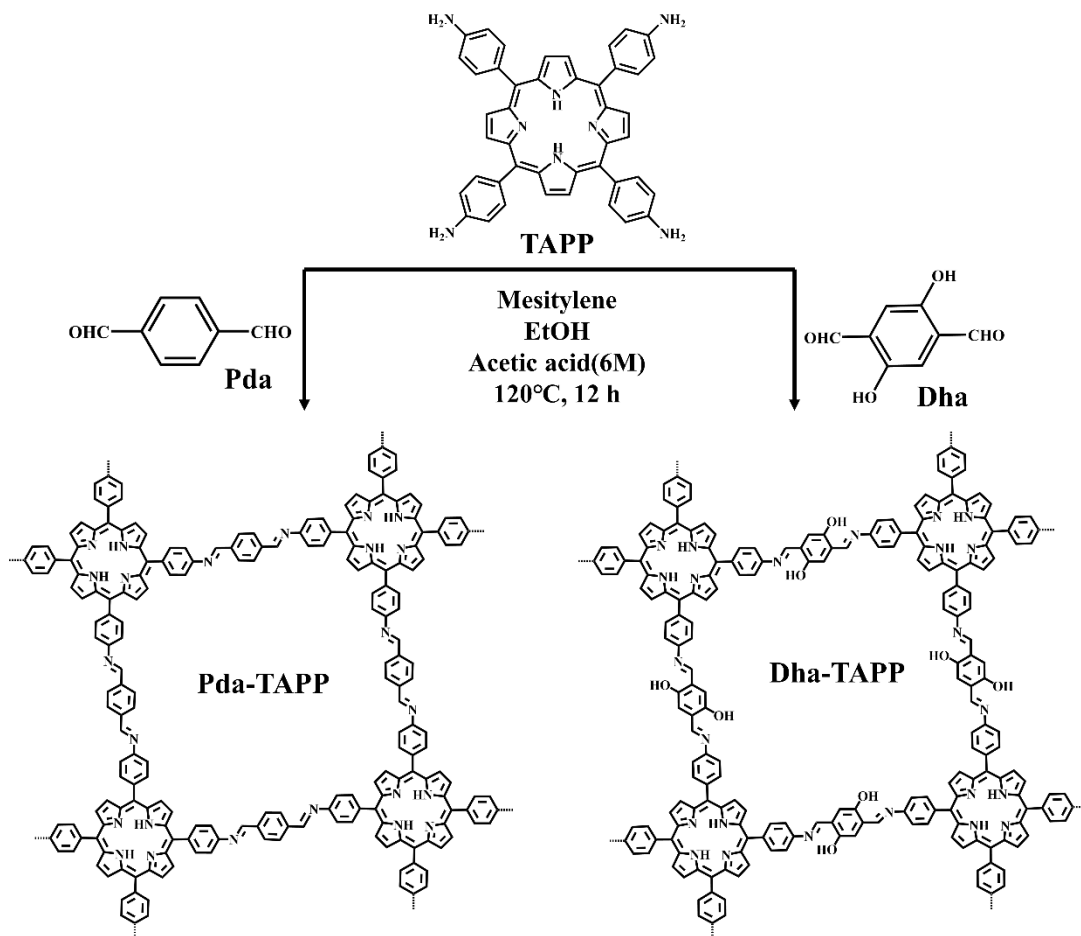
The electronic structures of Dha-TAPP and Pda-TAPP were studied by density functional theory (DFT), where the structure was optimized by the ω B97X-D3¹ functional and 6-31G**^{2,3} basis set using ORCA 5.0.2⁴. Moreover, the charge density difference was expressed as follows,

$$\Delta\rho = \rho(\text{Dha-TAPP}/\text{O}_2) - \rho(\text{Dha-TAPP}) - \rho(\text{O}_2)$$

where the terms at right hand are electron density of dimers between Dha-TAPP and O_2 , and monomers of Dha-TAPP and O_2 , respectively. Hirshfeld atomic charges, highest occupied molecular orbital (HOMO), lowest unoccupied molecular orbital (LUMO), and charge density difference were calculated by Multiwfn 3.8 (dev)⁵, whose input file was extracted from Molden from ORCA, and plotted by VESTA 3.5.5⁶. TD^{7,8}- ω B97X-D3/6-311G** were used to gain the excited states of studied molecules, whose electron-hole distributions and projected density of states (PDOS) were also calculated by Multiwfn.

Chemicals and materials.

4-[10,15,20-tris(4-aminophenyl)-21,24-dihydroporphyrin-5-yl]aniline (TAPP), terephthalaldehyde (Pda), mesitylene, and acetic acid were purchased from Shanghai Macklin Biochemical Co., Ltd. NaSO_4 , L(+)-Ascorbic acid, 1,4-Benzoquinone, KI, FeSO_4 , tert-Butanol, diclofenac sodium (DCF), ethylenediaminetetraacetic acid disodium salt (EDTA-2Na), and silver nitrate (AgNO_3), $\text{NH}_3 \cdot \text{H}_2\text{O}$, and potassium biphthalate were purchased from Sinopharm Chemical Reagent Co, Ltd. Ethanol, 2,5-dihydroxyterephthalaldehyde (Dha), ciprofloxacin, sulfamethoxazole, 30% H_2O_2 , and N,N-dimethylformamide (DMF) were purchased from Aladdin Chemical Reagent Co. Ltd. All reagents purchased are analytical grade or above and can be used without further purification.



S2. Supplementary Figures

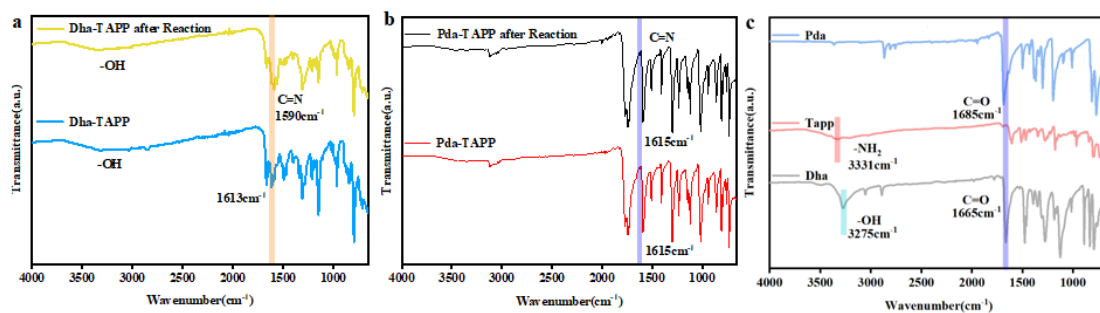


Figure S1. FT-IR spectra of (a) Dha-TAPP, Dha-TAPP after reaction and (b) Pda-TAPP, Pda-TAPP after reaction and (c) Pda, TAPP, Dha.

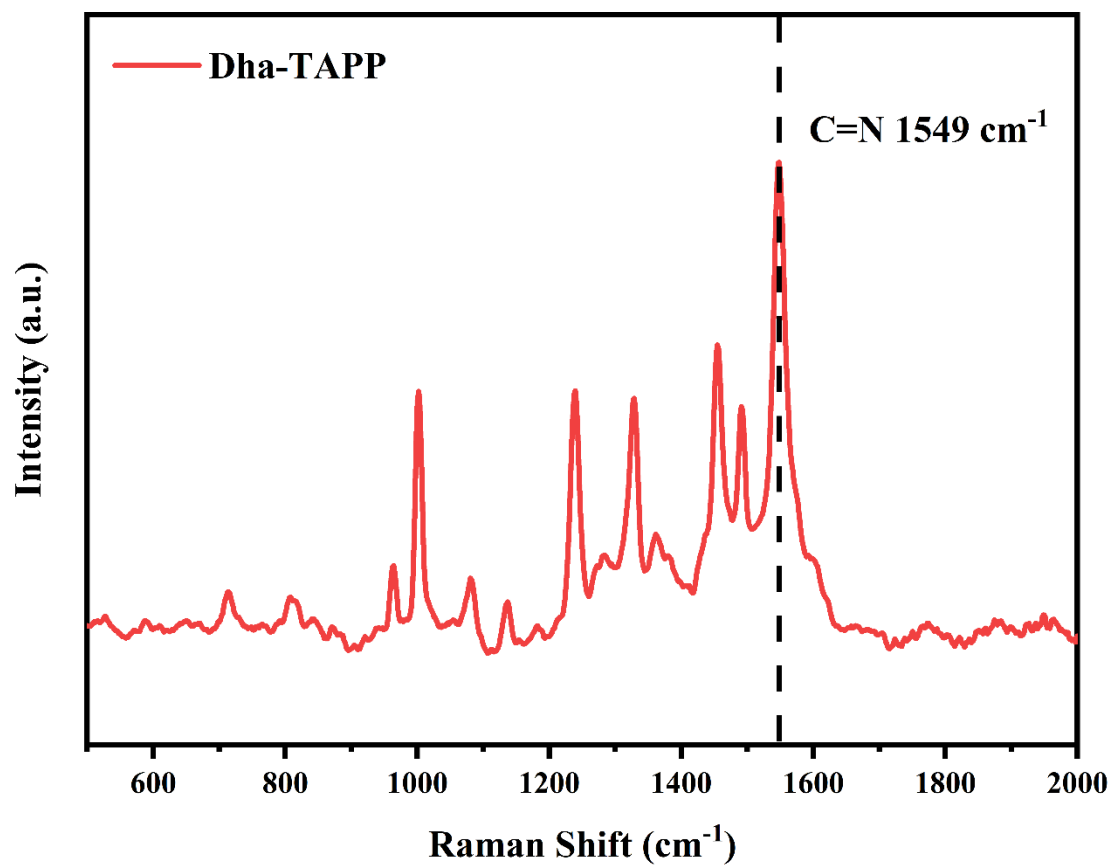


Figure S2. Raman spectra of Dha-TAPP.

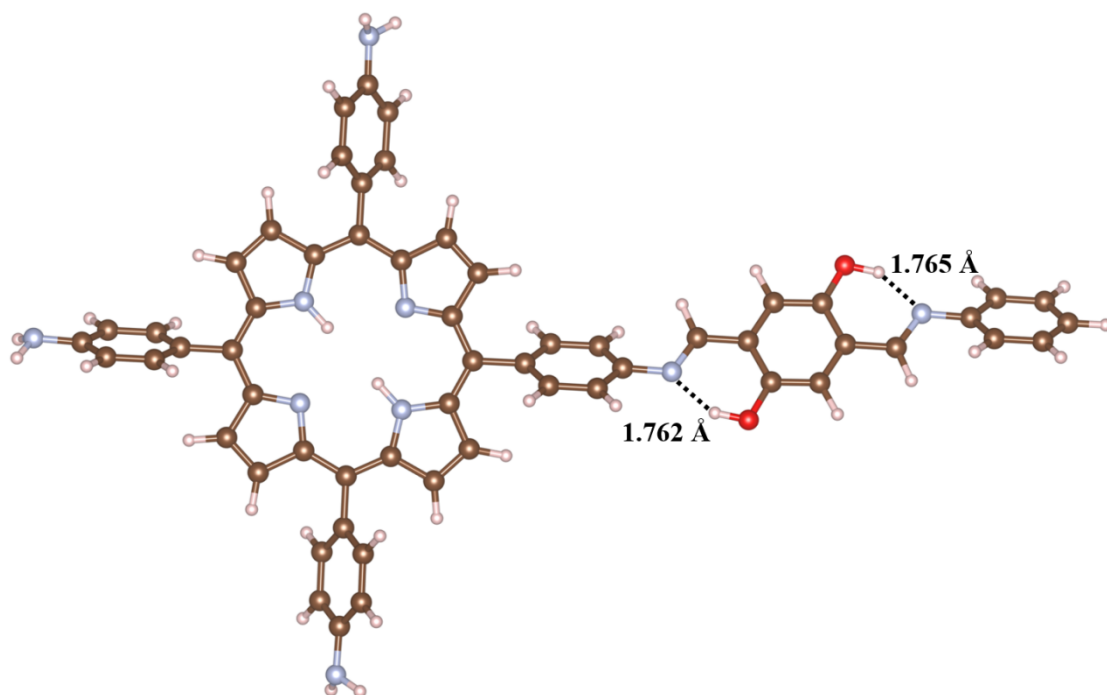


Figure S3. The optimized structures of Dha-TAPP at excited state, where the dash is intramolecular hydrogen bond and the unit is Å.

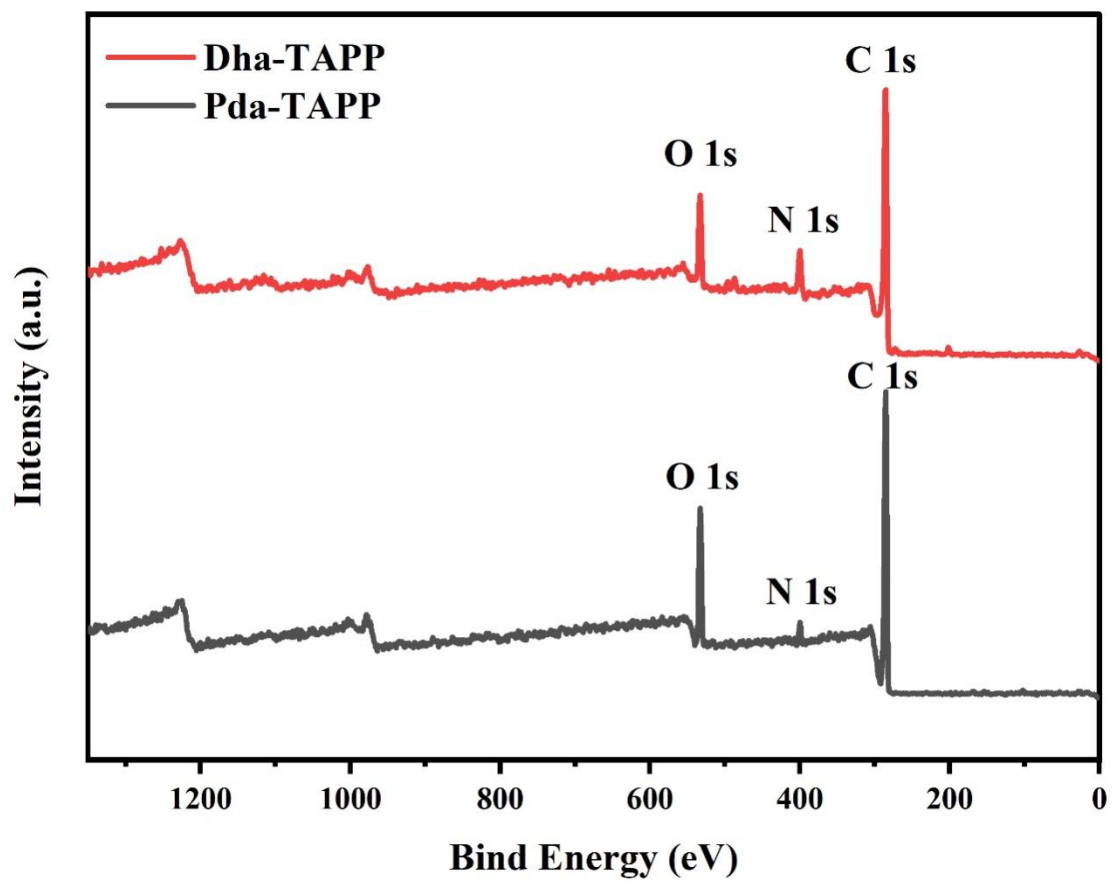


Figure S4. XPS survey of Pda-TAPP and Dha-TAPP.

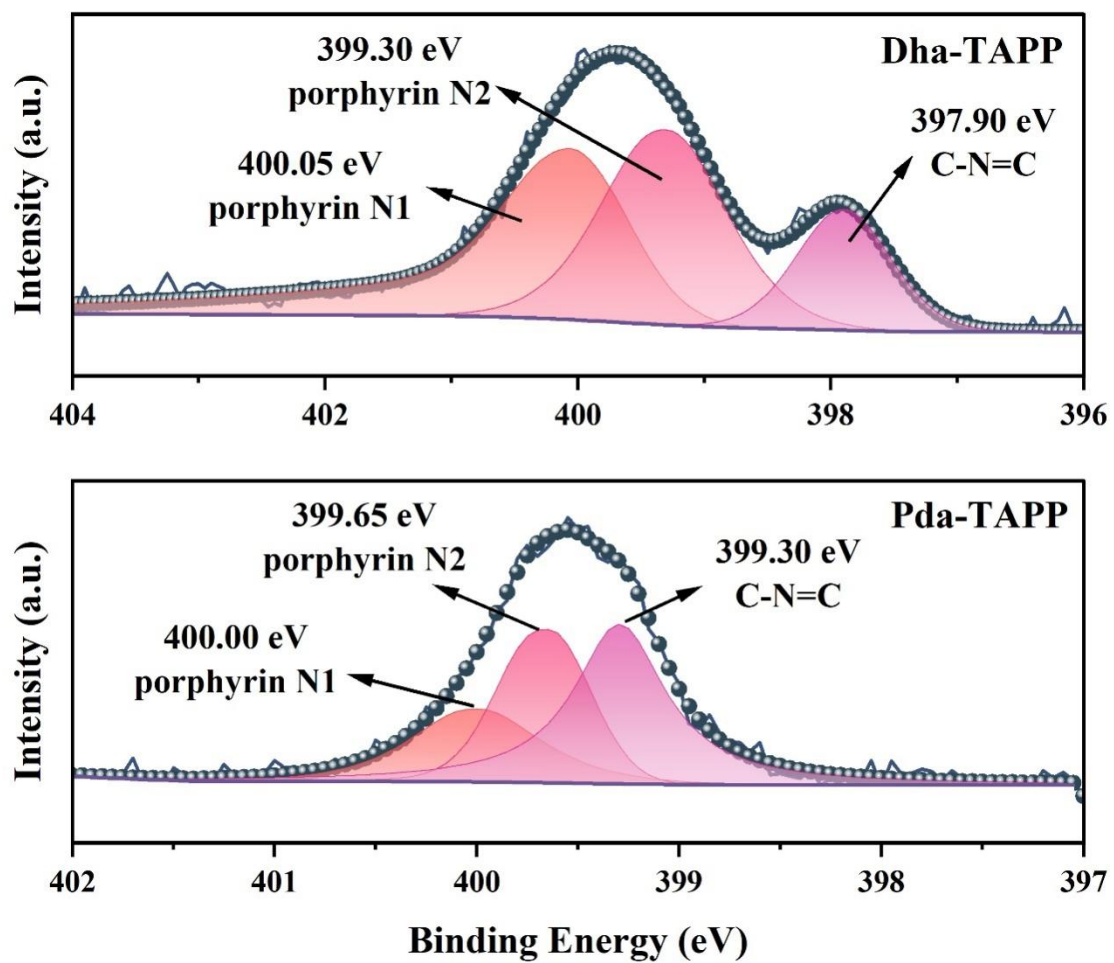


Figure S5. N 1s spectrum of Pda-TAPP and Dha-TAPP.

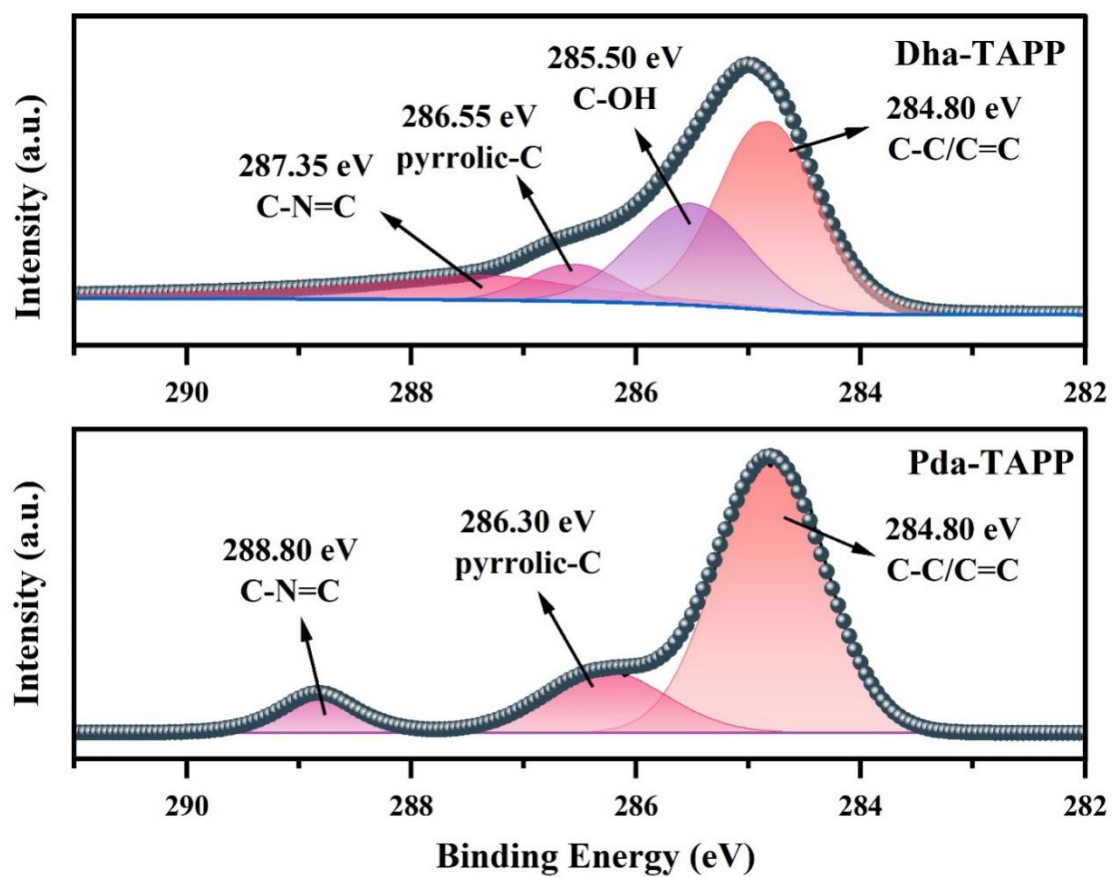


Figure S6. C 1s spectrum of Pda-TAPP and Dha-TAPP.

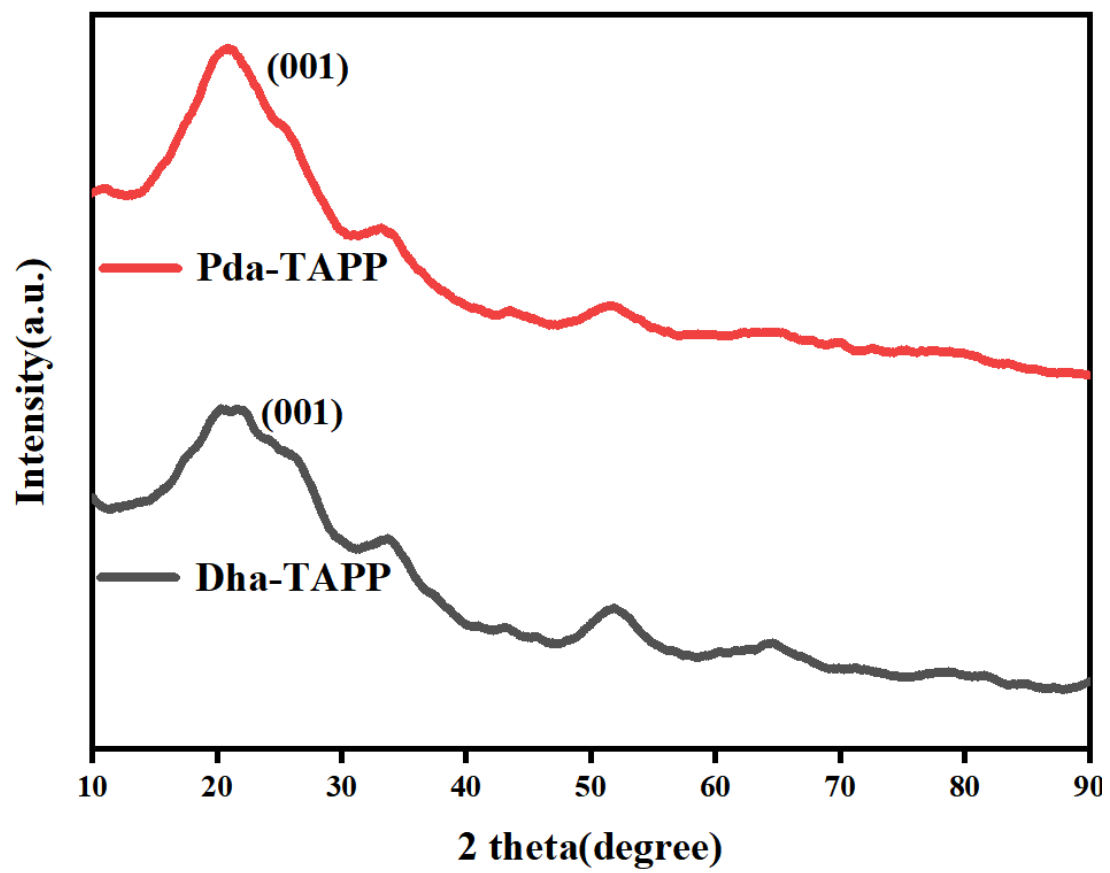


Figure S7. Wide angle XRD of Dha-TAPP and Pda-TAPP.

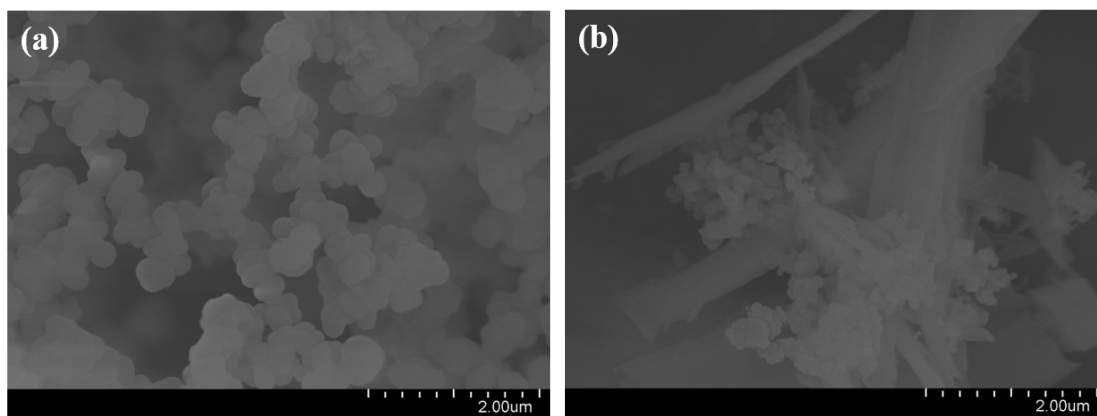


Figure S8. SEM images of a) Pda-TAPP and b) Dha-TAPP.

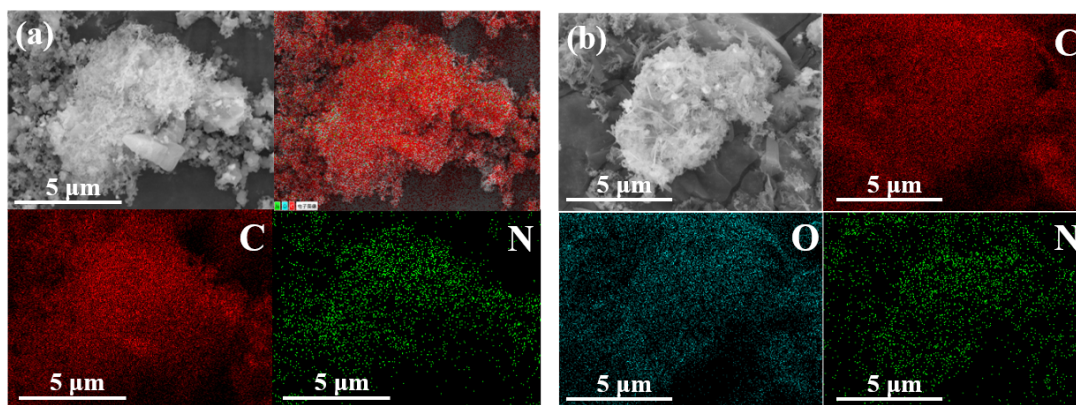


Figure S9. EDS mapping images of a) Pda-TAPP and b) Dha-TAPP.

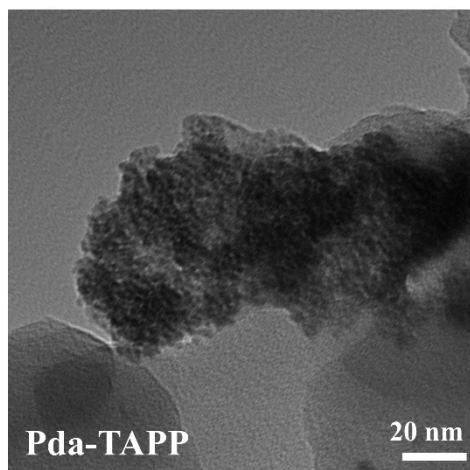


Figure S10. TEM images of Pda-TAPP.

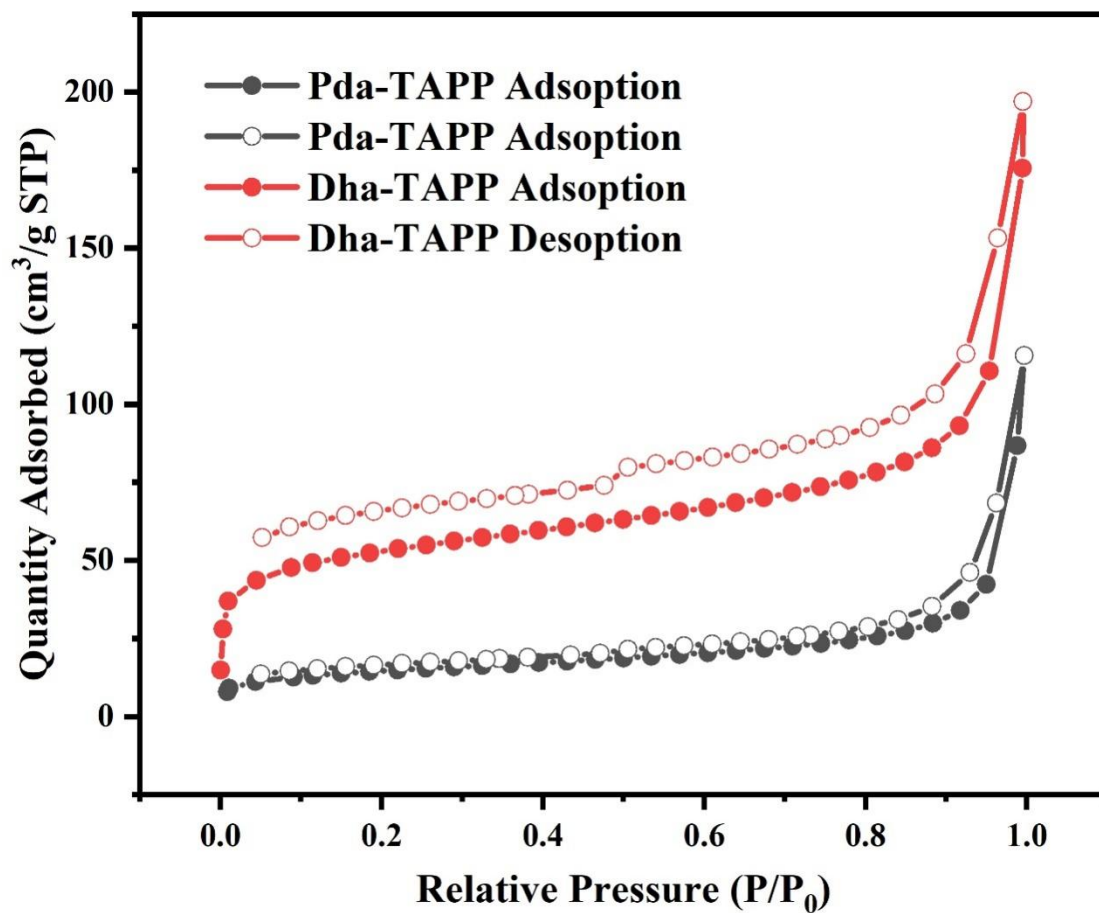


Figure S11. N₂ adsorption and desorption curves of Pda-TAPP and Dha-TAPP.

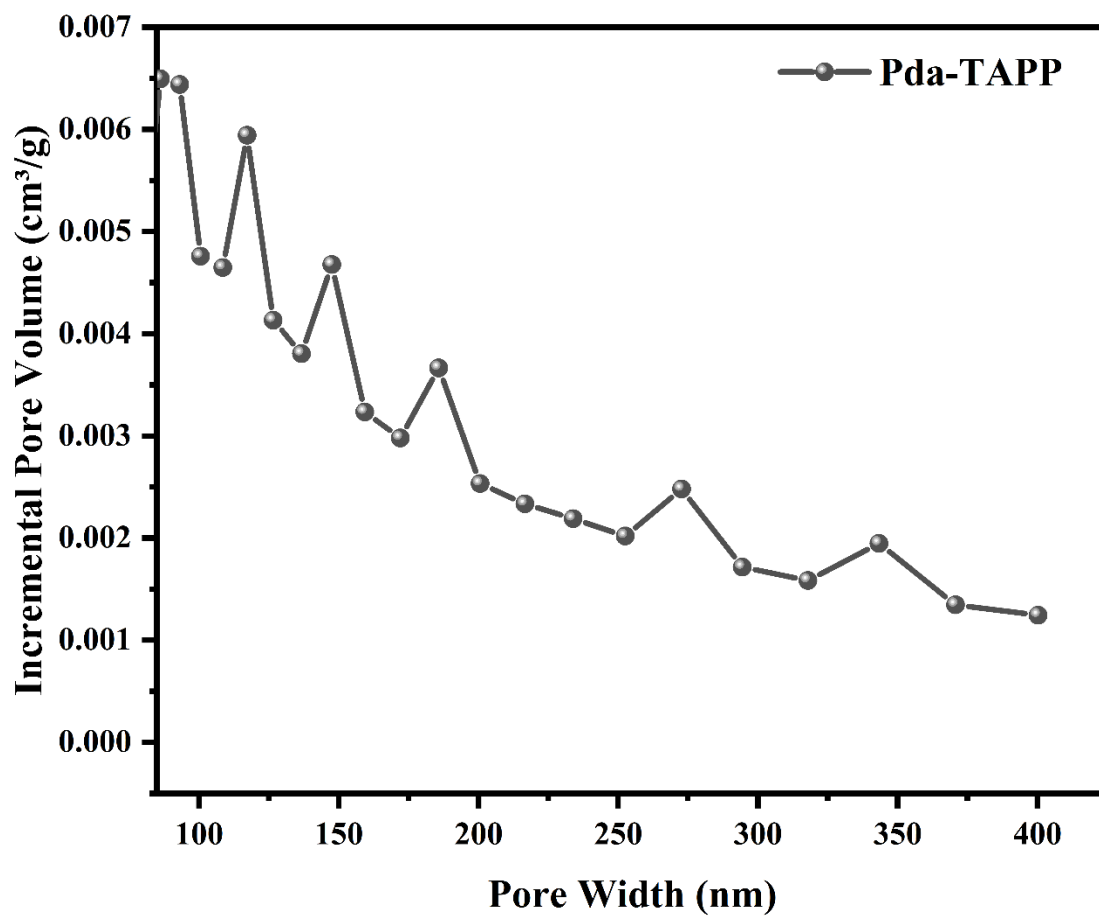


Figure S12. Incremental pore volume curves of Pda-TAPP.

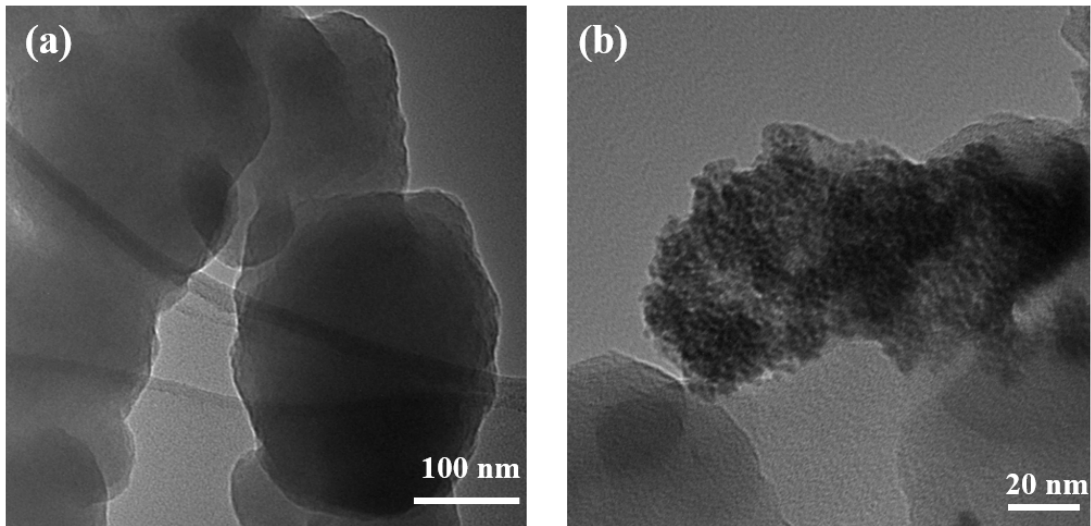


Figure S13. TEM images of Pda-TAPP.

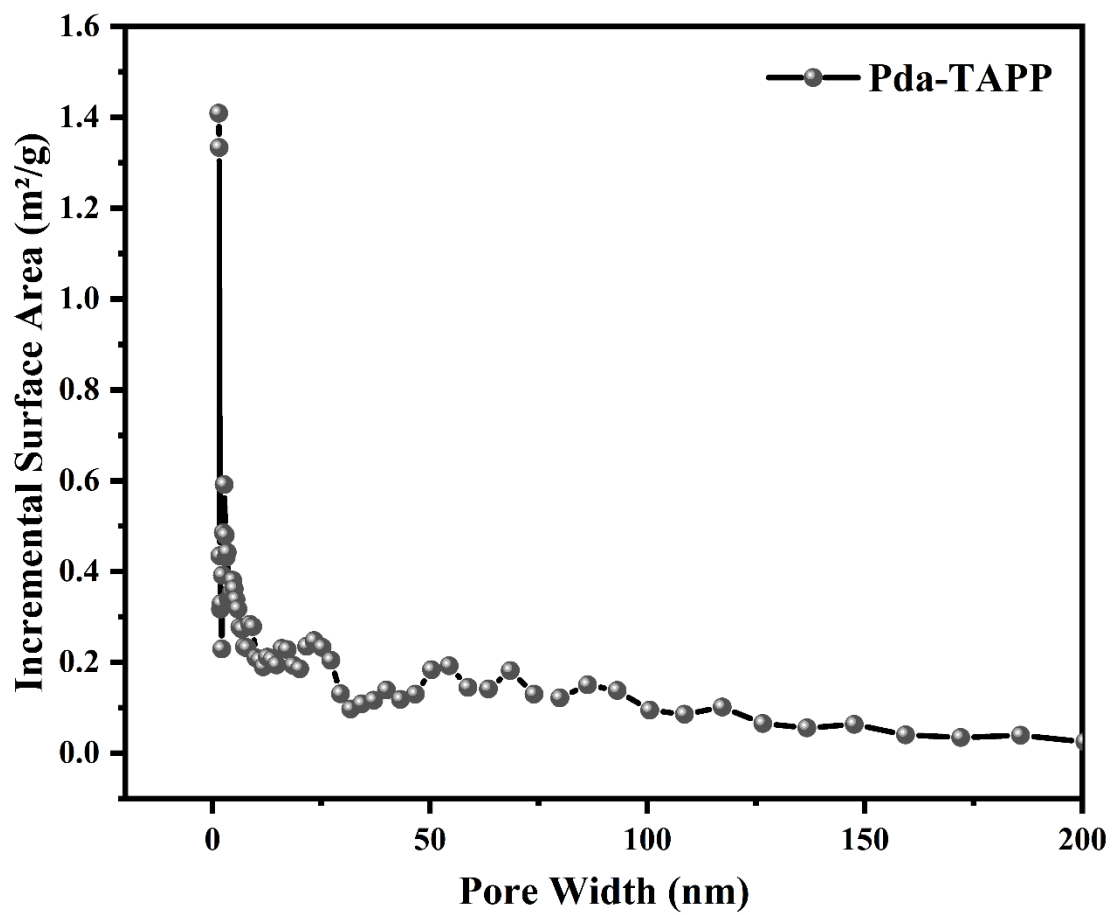


Figure S14. Incremental surface area vs. pore width of Pda-TAPP.

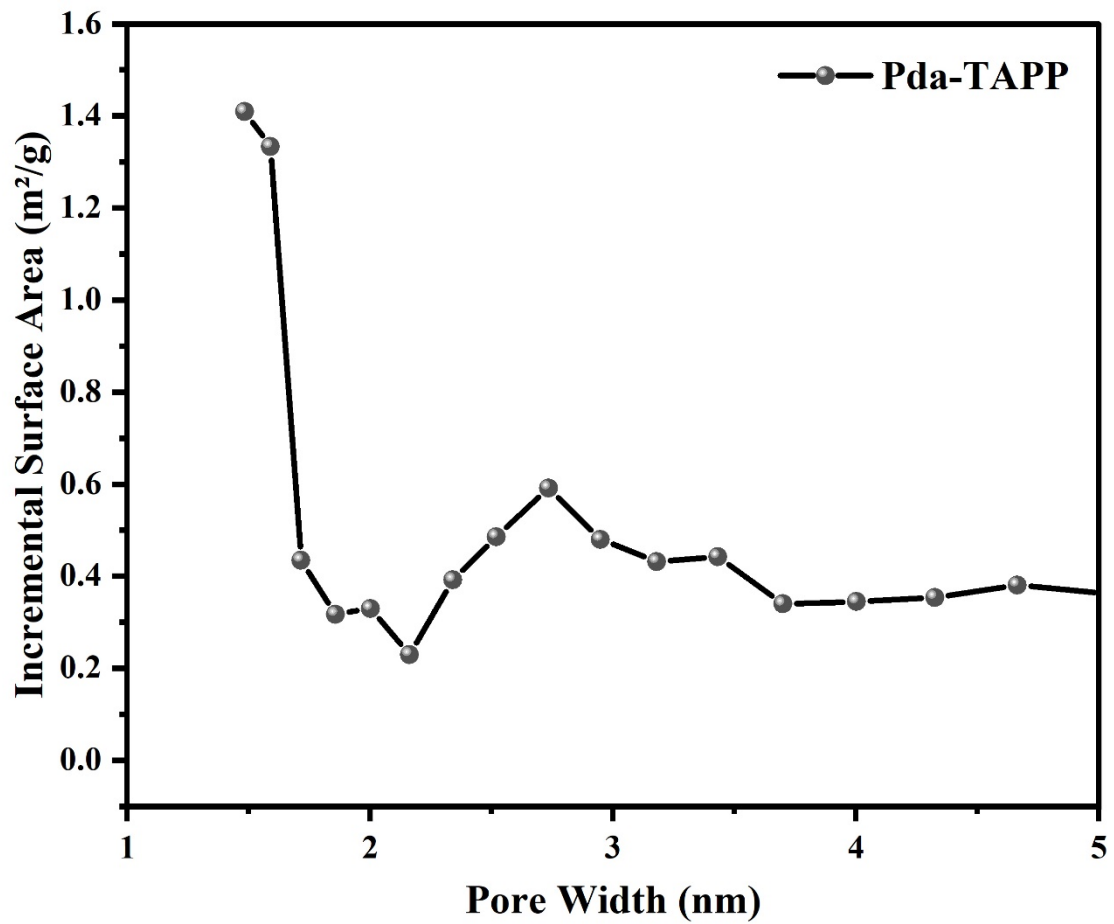


Figure S15. Incremental surface area vs. pore width of Pda-TAPP.

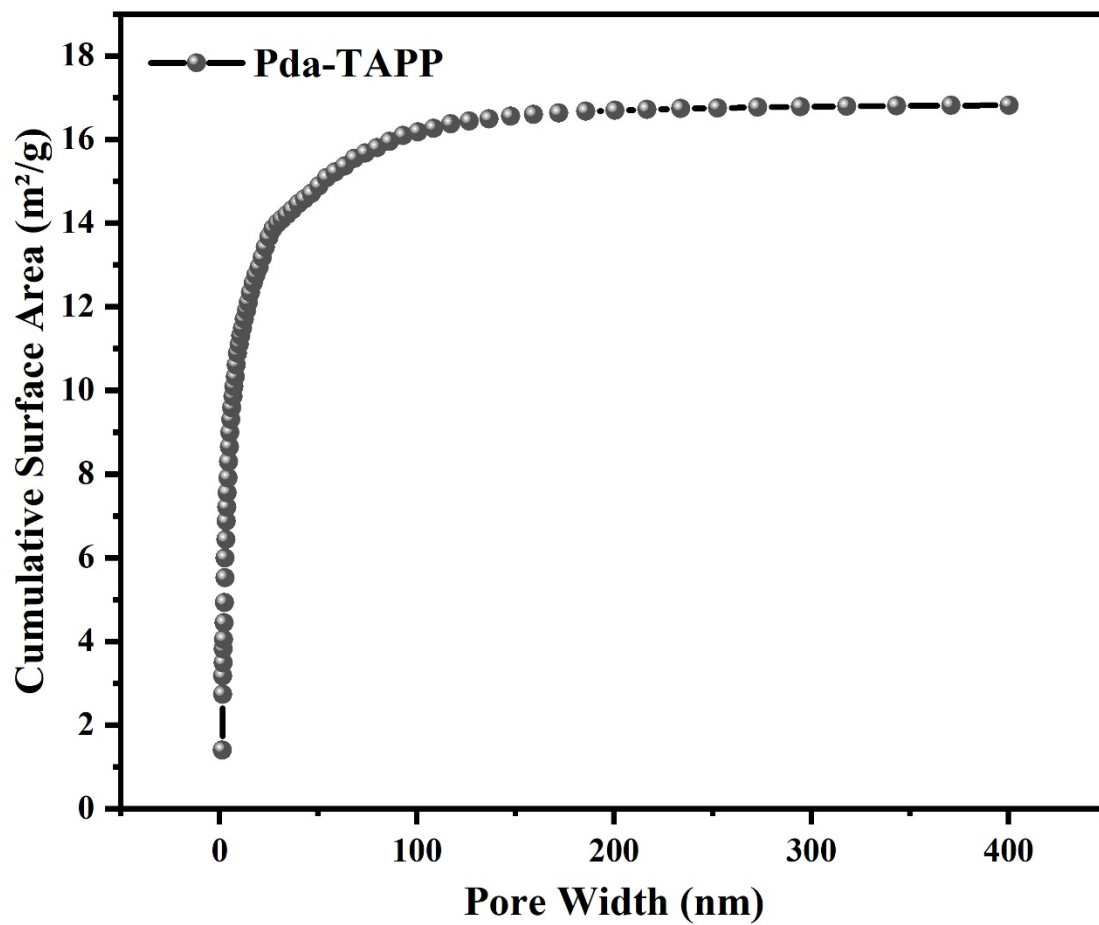


Figure S16. Cumulative surface area vs. pore width of Pda-TAPP.

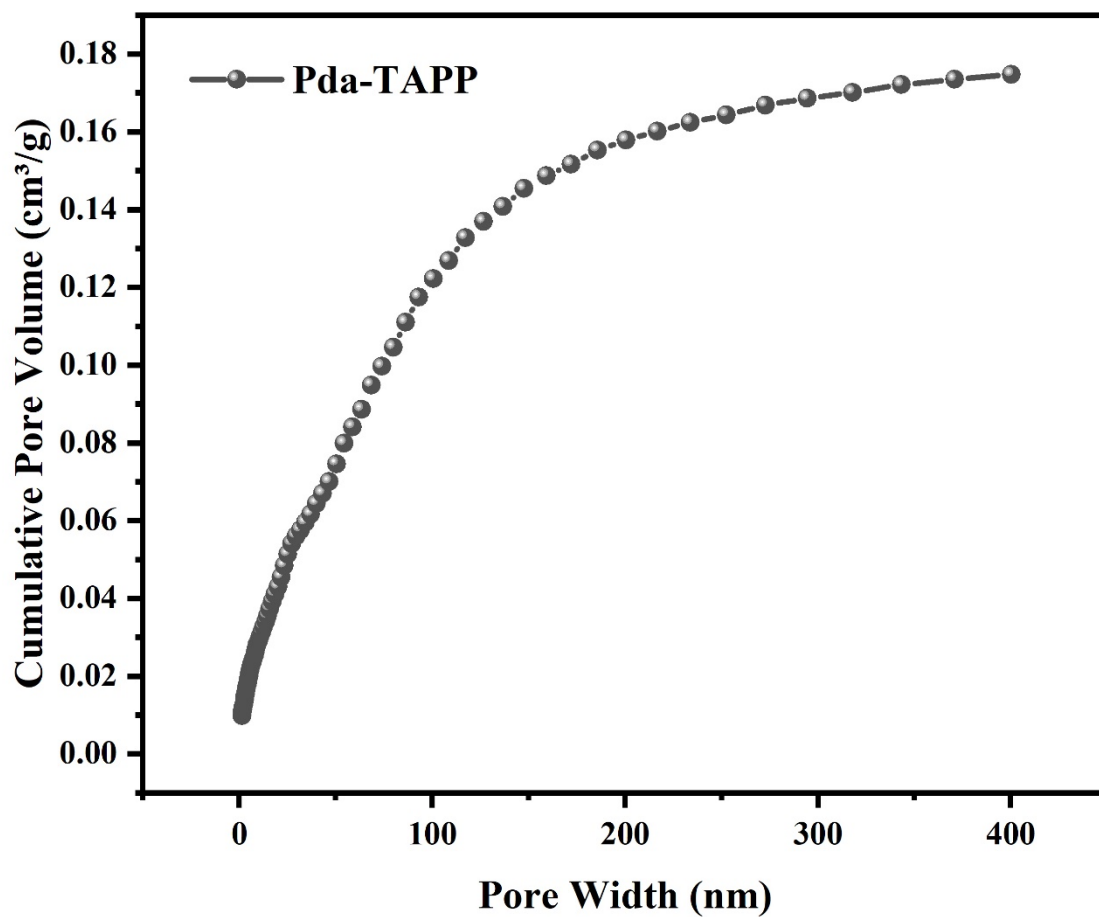


Figure S17. Cumulative pore volume vs. pore width of Pda-TAPP.

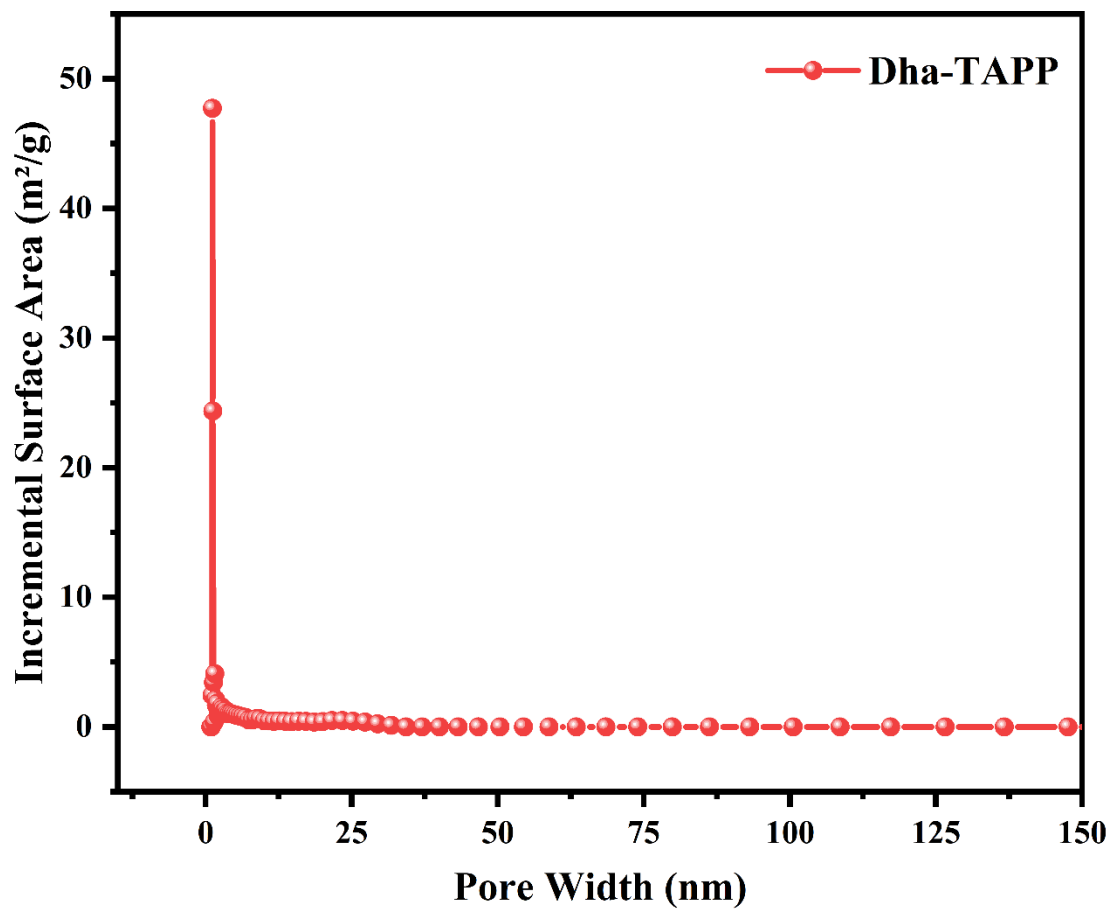


Figure S18. Incremental surface area vs. pore width of Dha-TAPP.

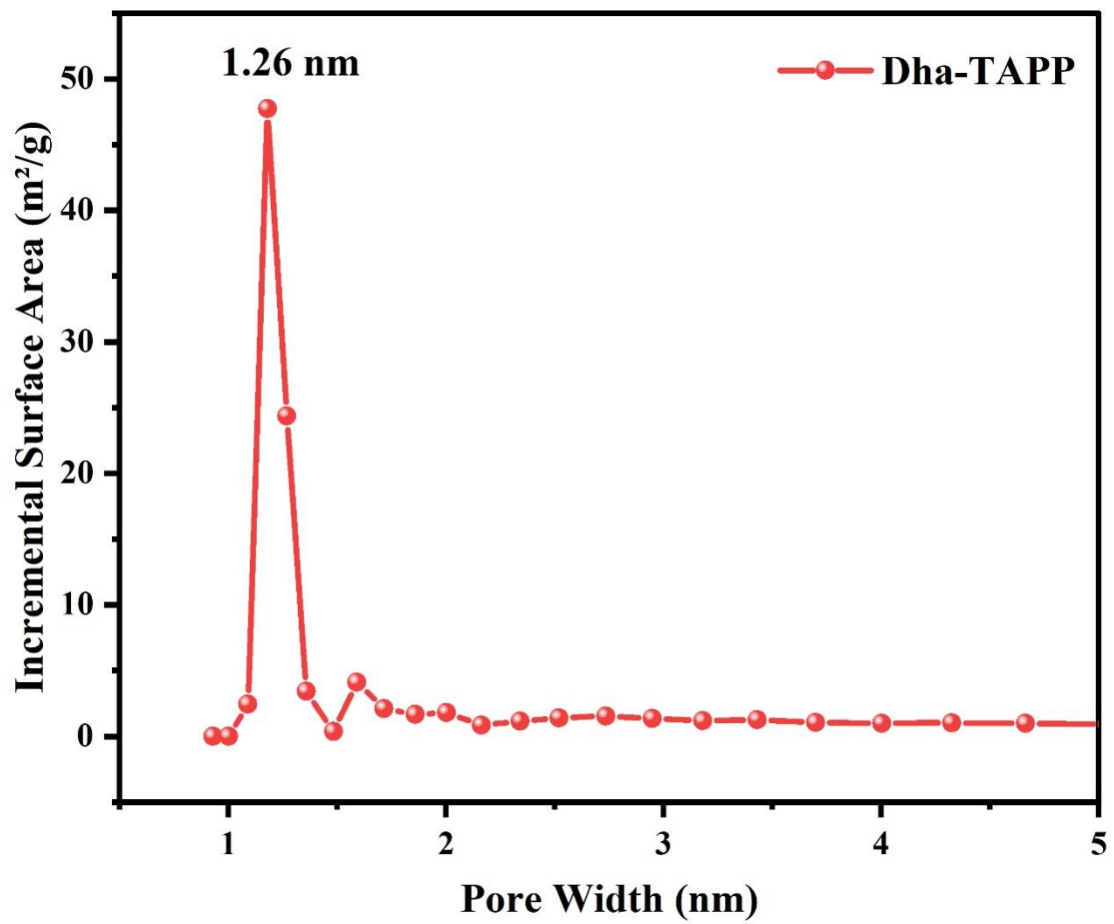


Figure S19. Incremental surface area vs. pore width of Dha-TAPP.

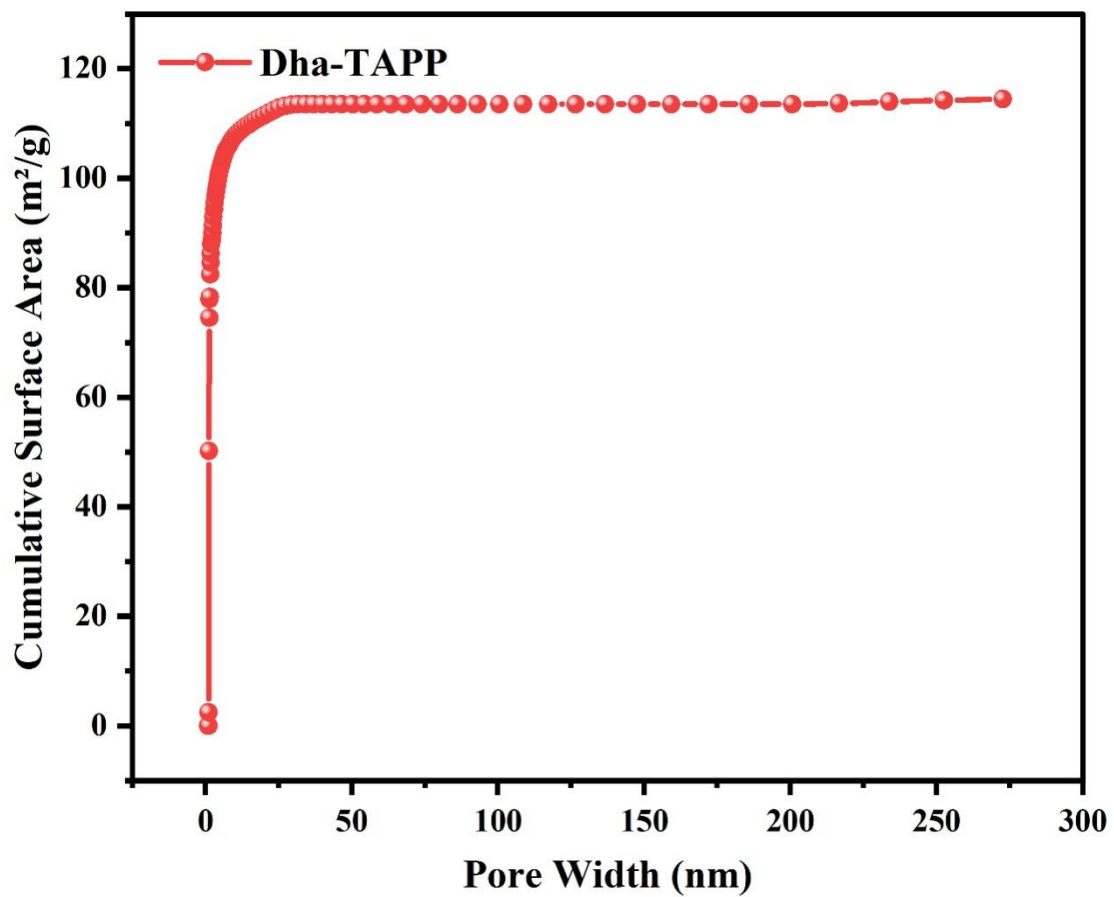


Figure S20. Cumulative surface area vs. pore width of Dha-TAPP.

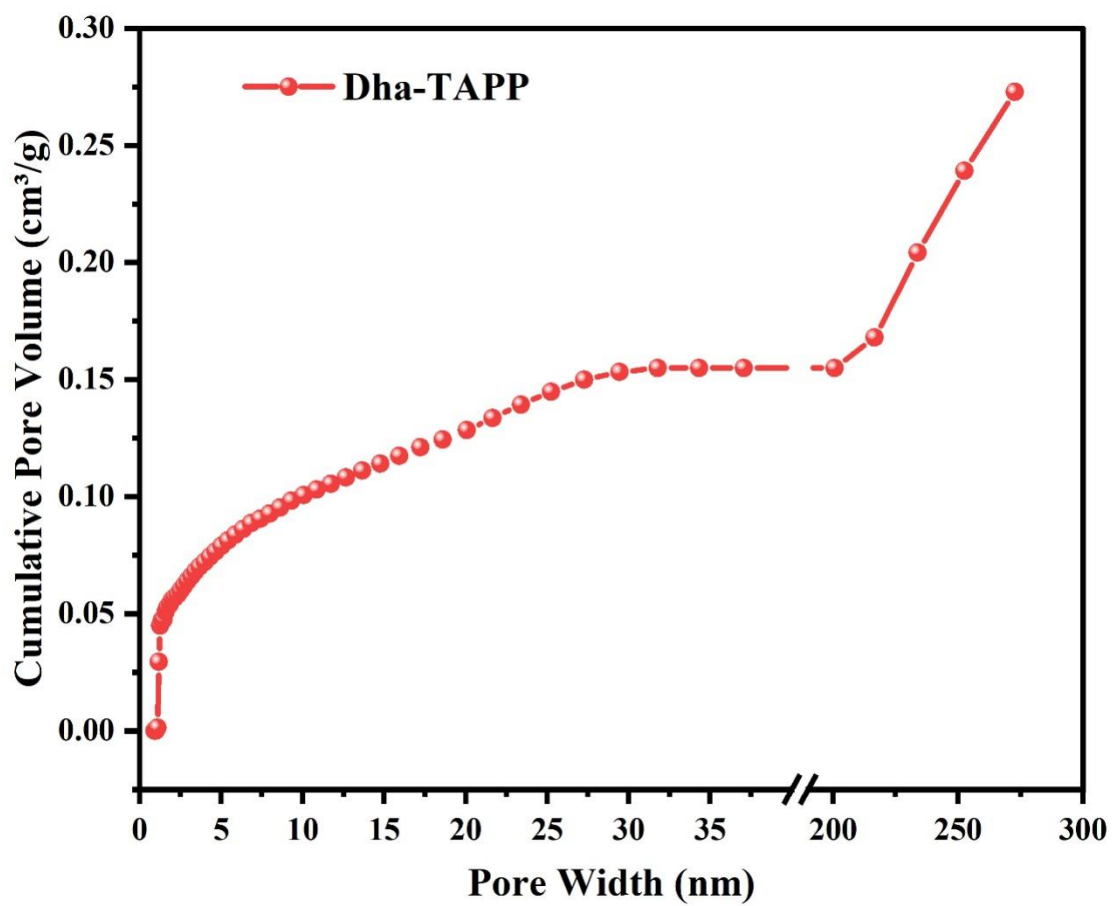


Figure S21. Cumulative pore volume vs. pore width of Dha-TAPP.

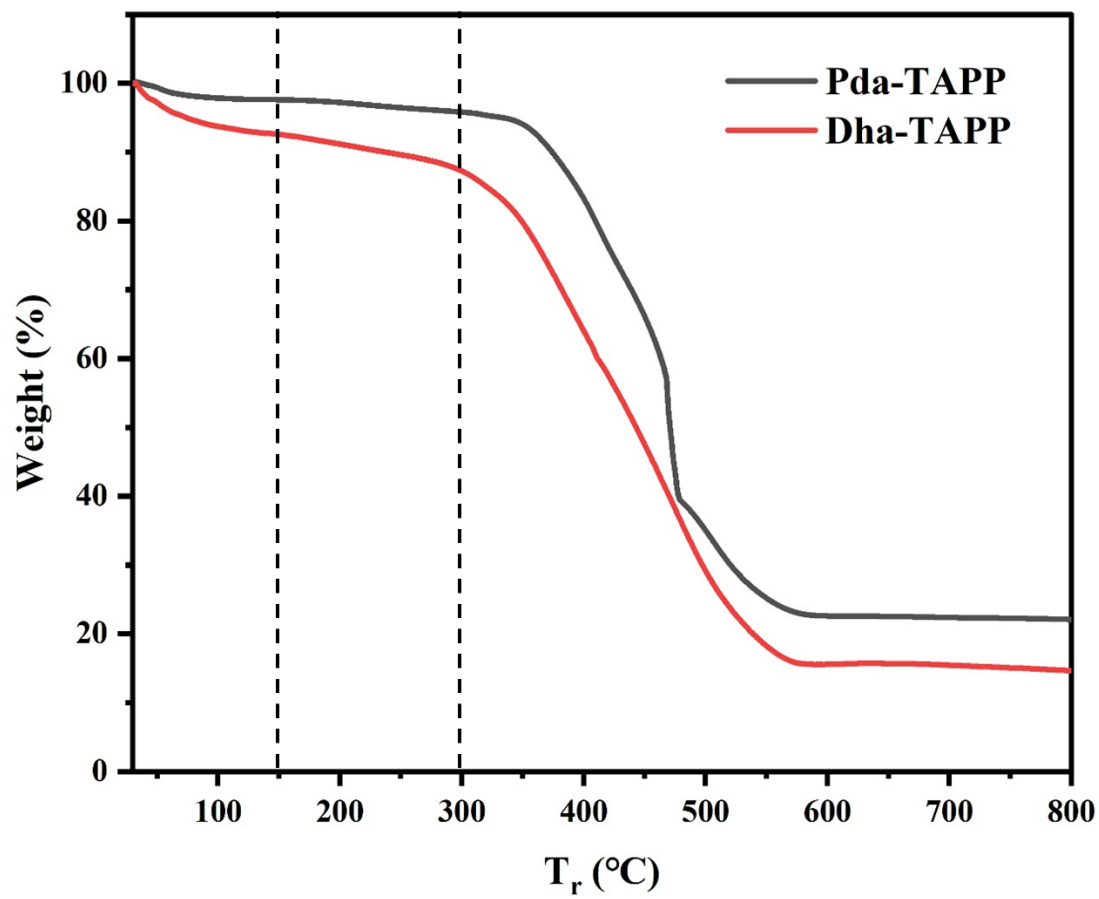


Figure S22. Thermogravimetric loss curves of Pda-TAPP and Dha-TAPP.

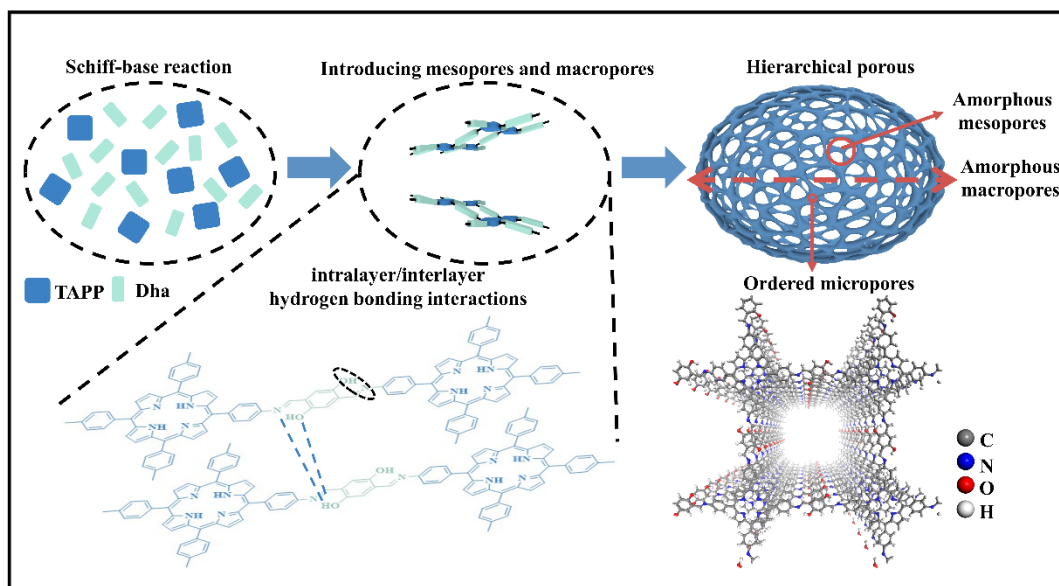


Figure S23. The transformation process scheme of synthetic hierarchical porous .

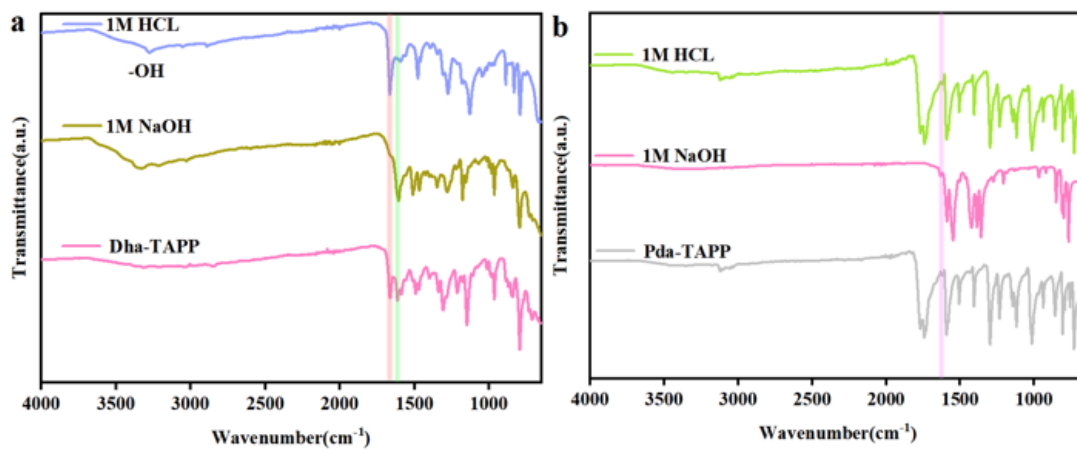


Figure S24. (a) Dha-TAPP after being immersed in 1M NaOH and 1M H₂SO₄ for 12h and (b) Pda-TAPP after being immersed in 1M NaOH and 1M H₂SO₄ for 12h.

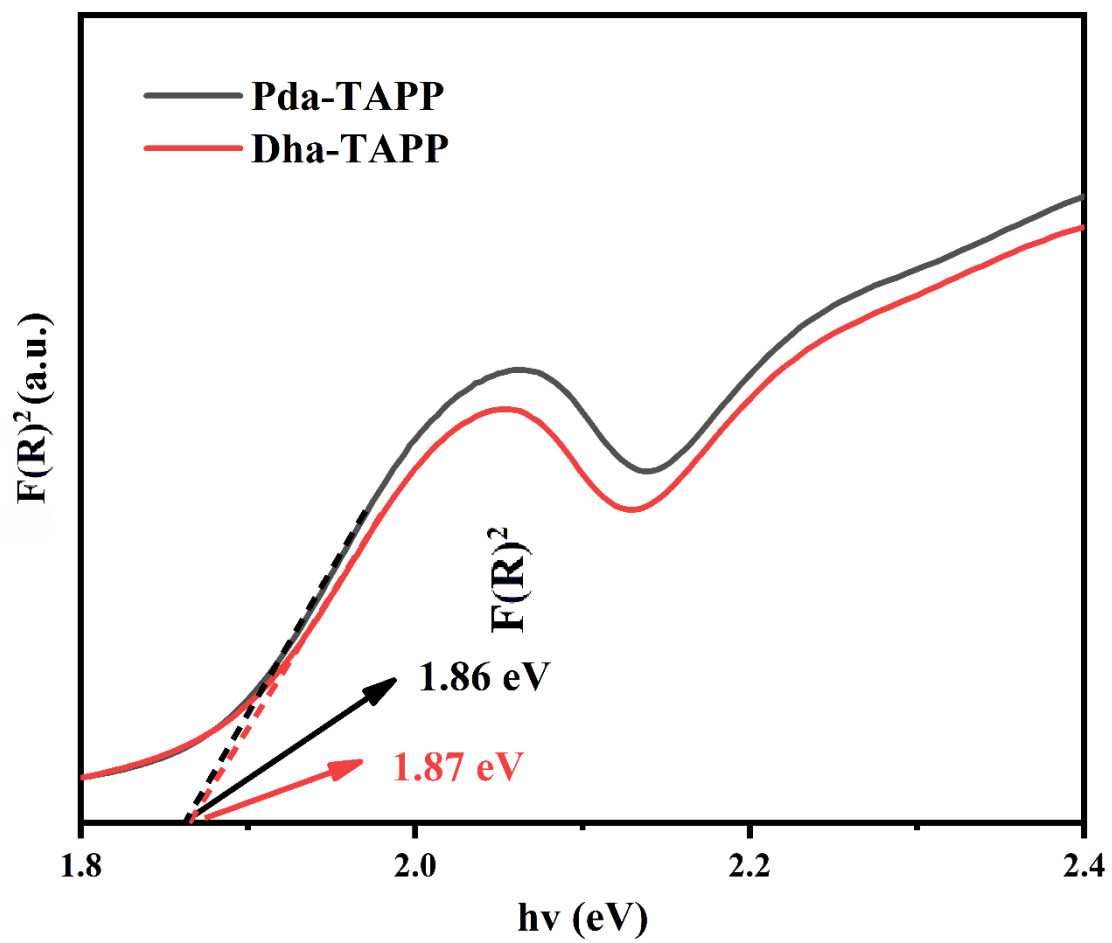


Figure S25. Photographs of Pda-TAPP and Dha-TAPP.

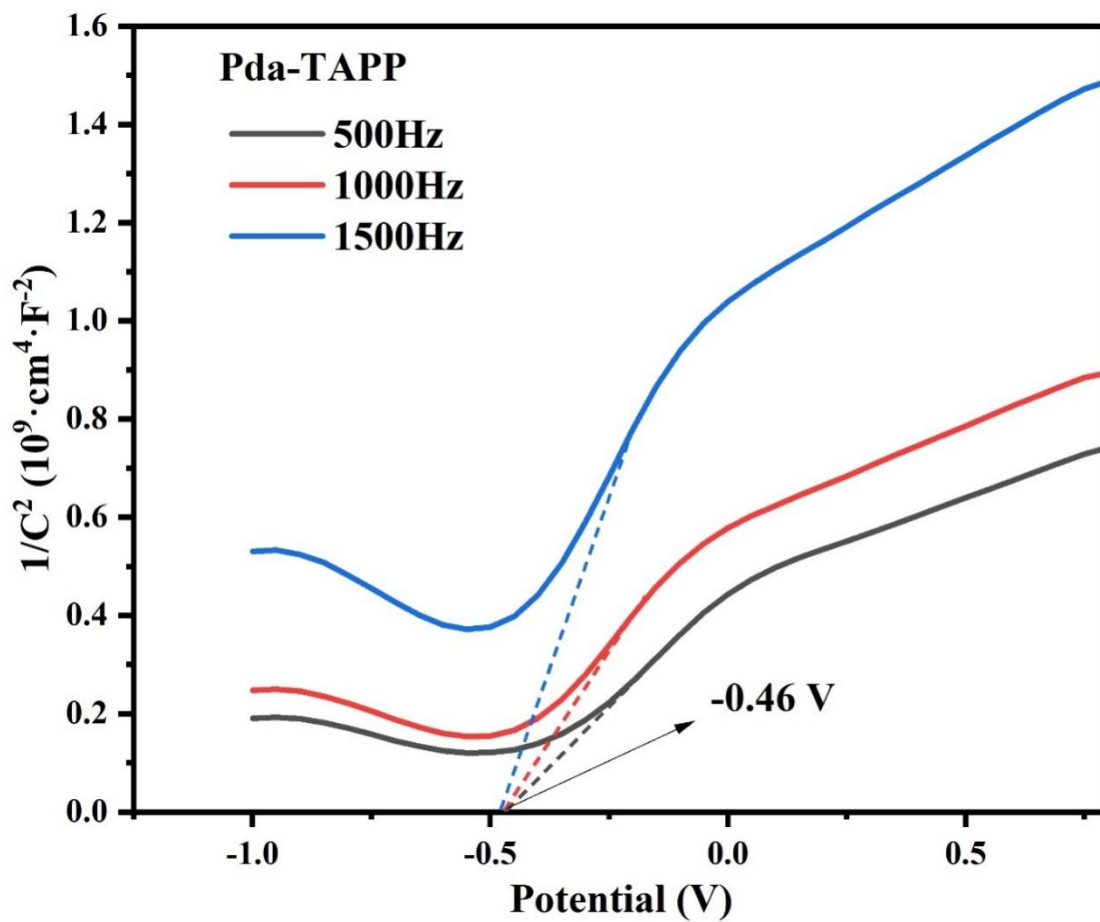


Figure S26. Mott-Schottky curves at three different frequencies of Pda-TAPP.

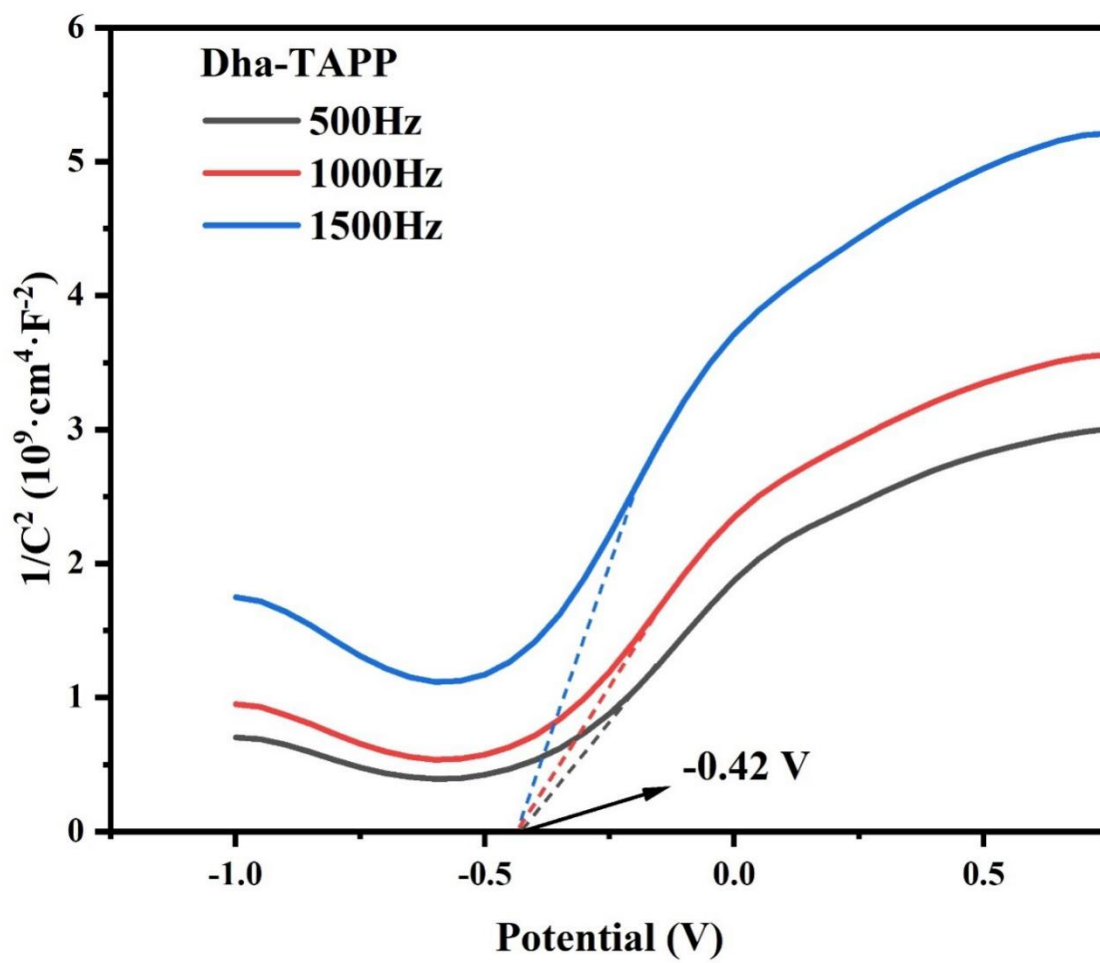


Figure S27. Mott-Schottky curves at three different frequencies of Dha-TAPP.

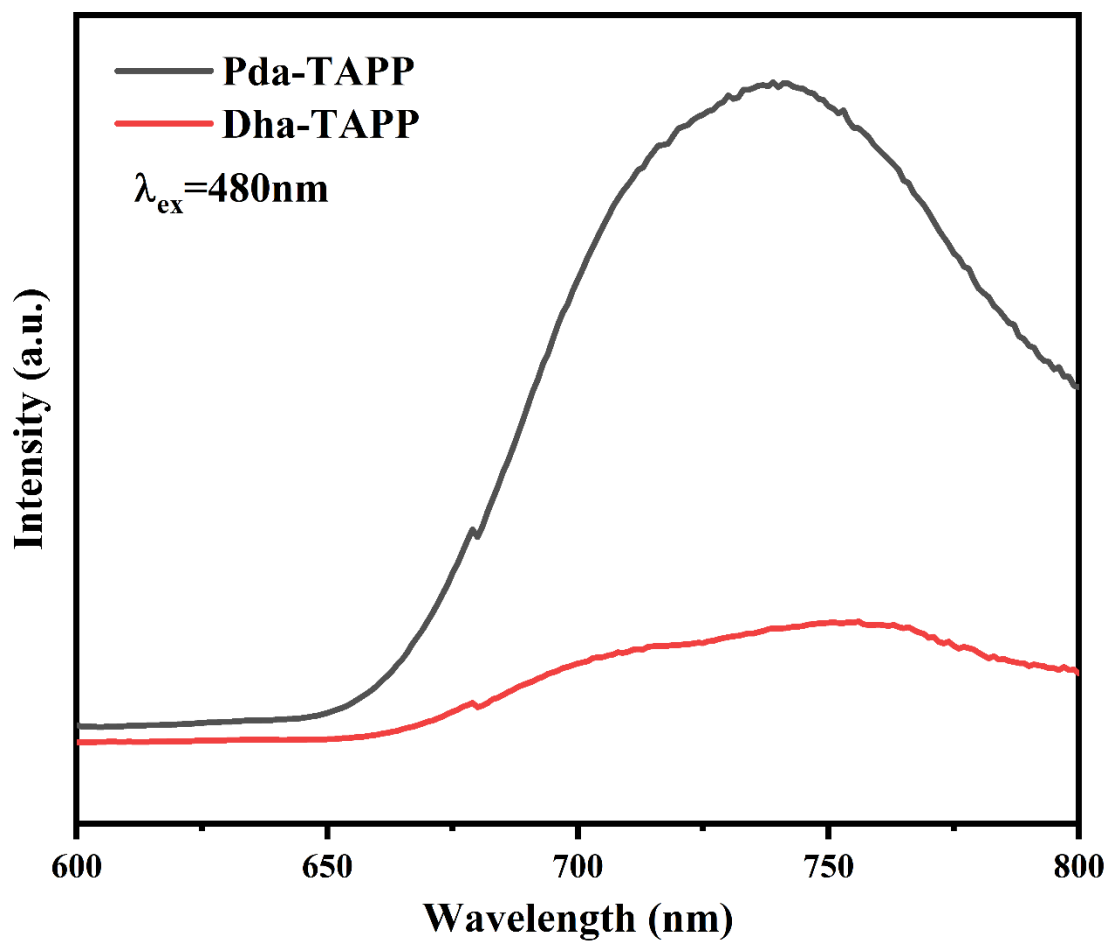


Figure S28. PL spectra of Pda-TAPP and Dha-TAPP, with the excitation wavelength of 480 nm.

(a) CA=18.74

Pda-TAPP (b) CA=19.41

Dha-TAPP

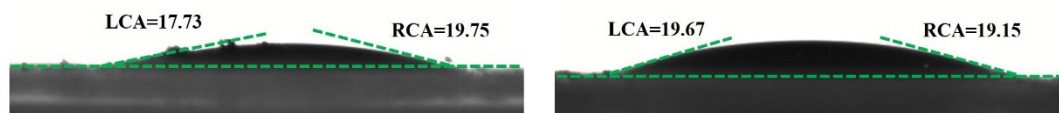


Figure S29. Contact angle of Pda-TAPP and Dha-TAPP.

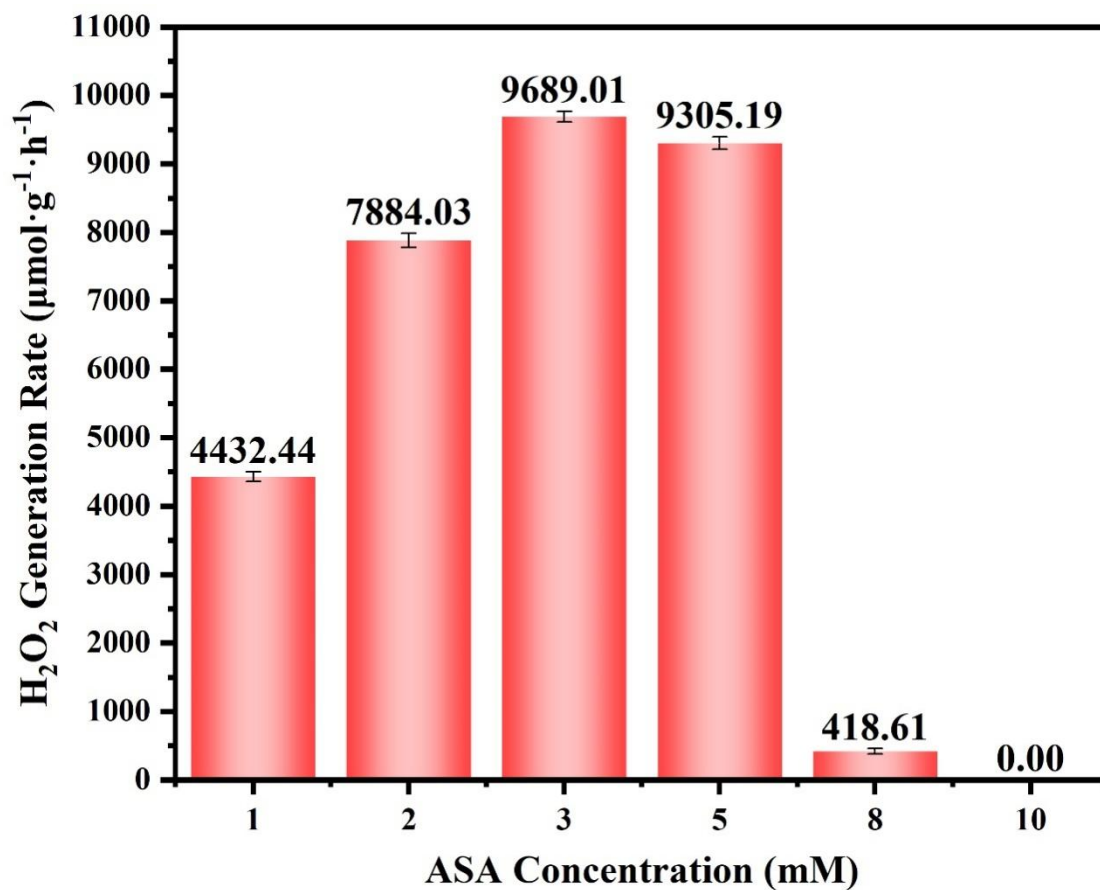


Figure S30. Photocatalytic synthesis of H₂O₂ by Dha-TAPP at different ASA concentrations

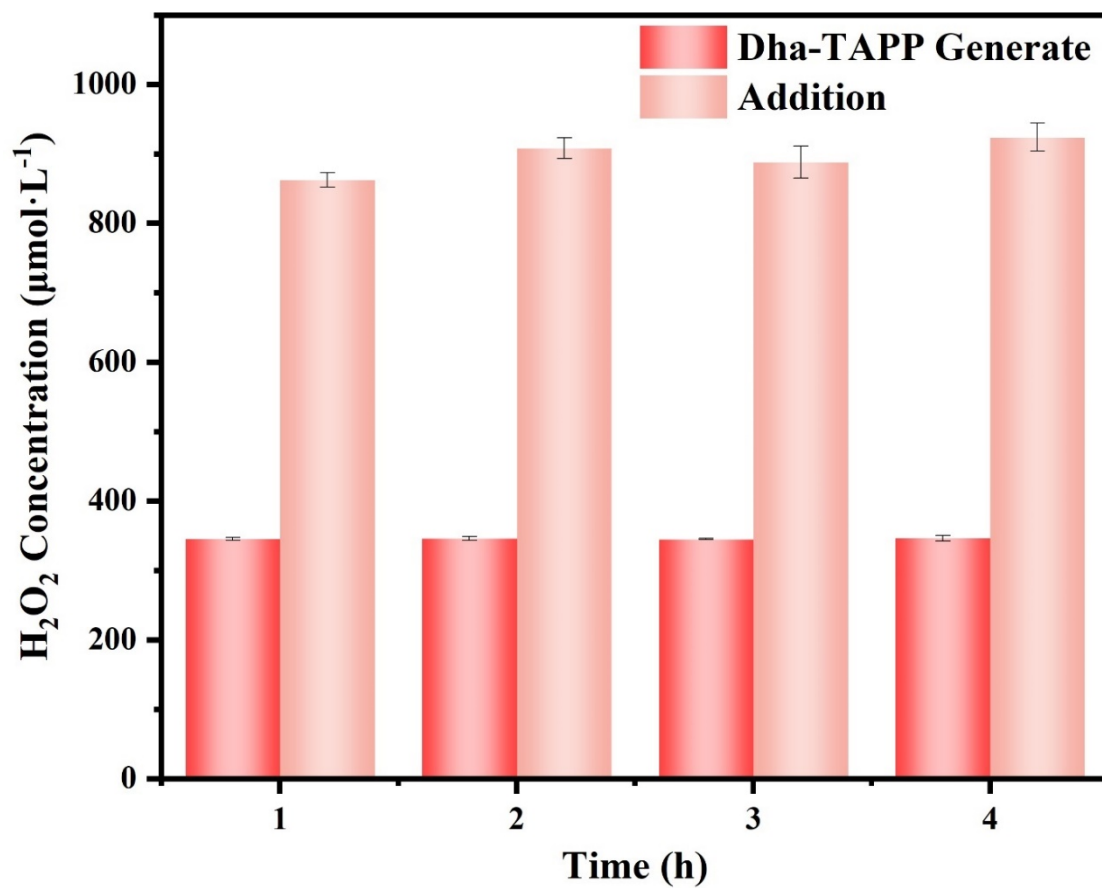


Figure S31. Decomposition of Dha-TAPP self-produced H₂O₂ (346 μM) and added H₂O₂ (1 mM) under dark conditions.

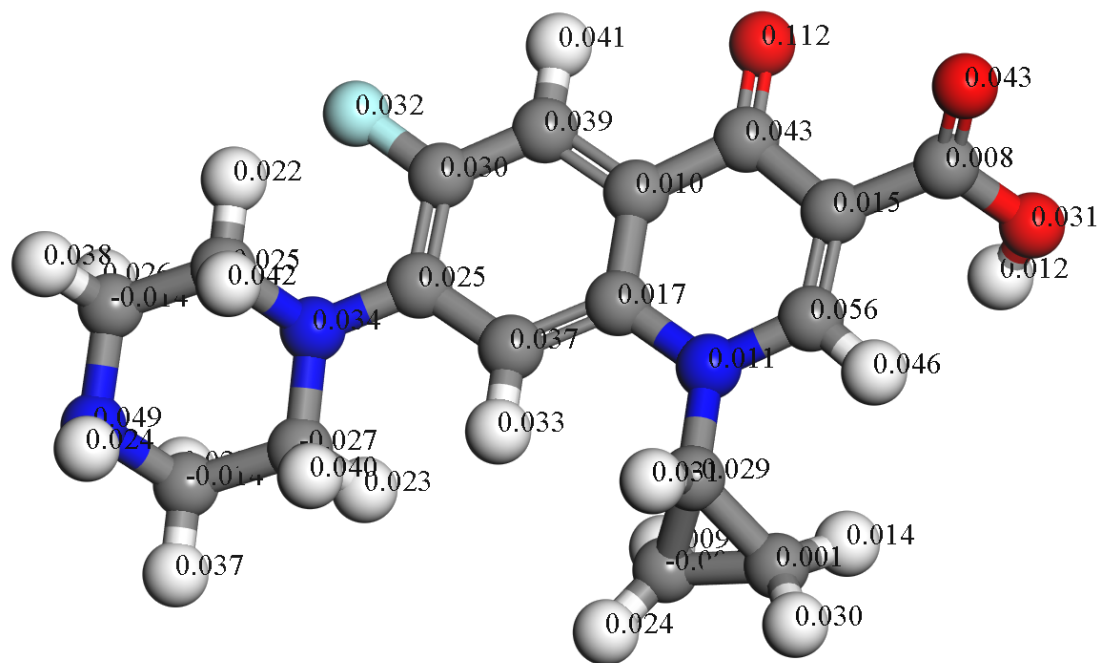


Figure S32. The Fukui index of CIP.

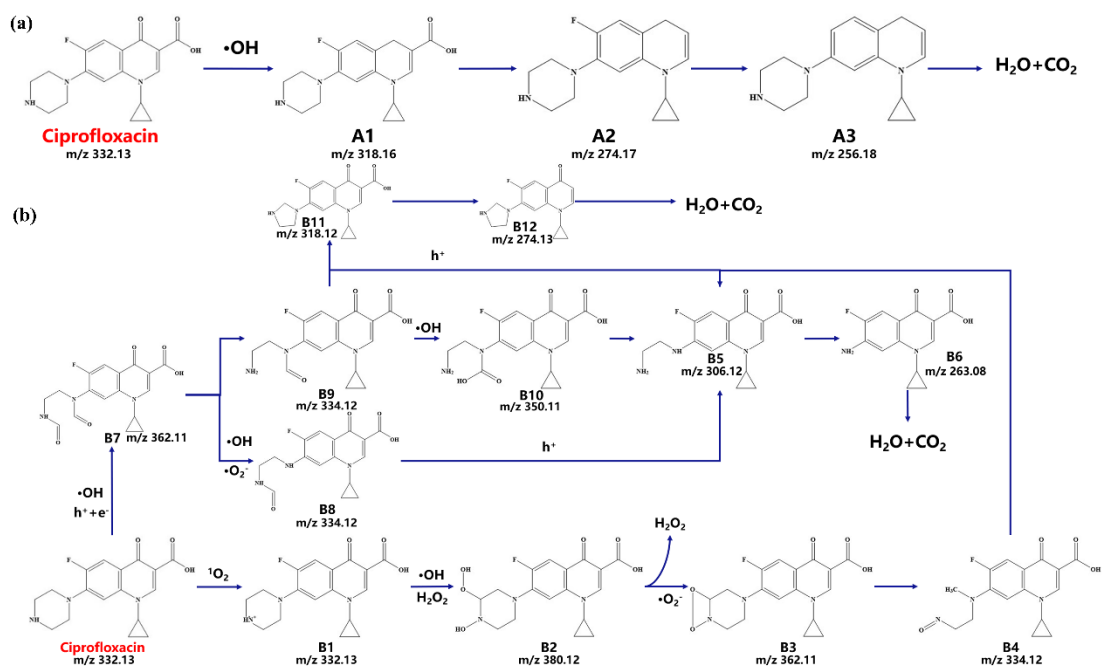


Figure S33. a) Degradation pathway of CIP: attacking the O atom in the CIP quinolone ring structure. b) Degradation pathway of CIP: attacking N atom of CIP pyrimidine ring.

Specifically speaking, for the degradation path A, the $\cdot\text{OH}$ produced during the photo-self-Fenton process attacked the O atom in the quinolone ring, leading to decarboxylation and defluorination, ultimately mineralizing into H_2O and CO_2 . For degradation pathway B, in addition to the action of $\cdot\text{OH}$ generated from H_2O_2 conversion, photogenerated electrons and holes, as well as other ROS ($\cdot\text{O}_2^-$ and $^1\text{O}_2$), all participate in the degradation process of CIP. Among them, $\cdot\text{OH}$, photogenerated electrons and holes jointly attack the pyrimidine ring to produce intermediate product B7, which is then further elaborately mineralized by the actions of $\cdot\text{OH}$ and $\cdot\text{O}_2^-$. Importantly, singlet oxygen plays a crucial role in the degradation process by activating CIP to produce intermediate B1, which is further degraded by the combined action of the ROS ($\cdot\text{OH}$, $\cdot\text{O}_2^-$, and H_2O_2) (Figure S33a, b).

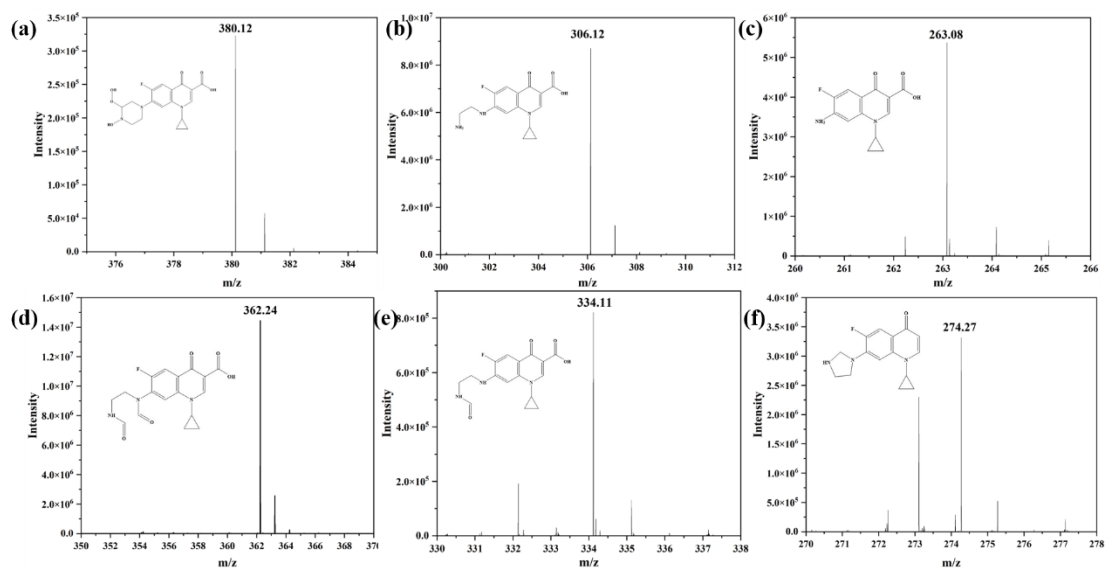


Figure S34. MS spectrum of some intermediates.

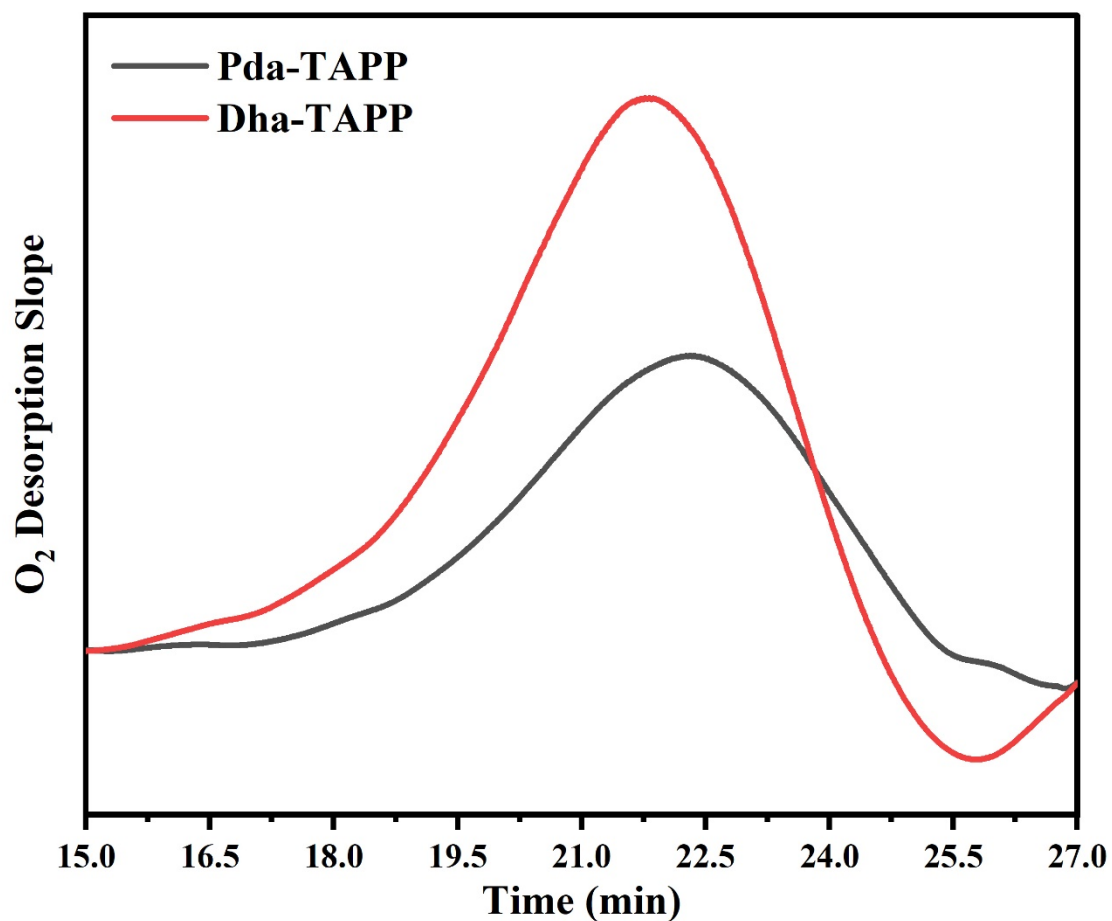


Figure S35. O₂ desorption slope plots (differential O₂-TPD curves) for Pda-TAPP and Dha-TAPP.

Figure S35 clearly indicates that the desorption slope of Dha-TAPP is significantly greater than that of Pda-TAPP, indicating its stronger O₂ adsorption conversion capability.

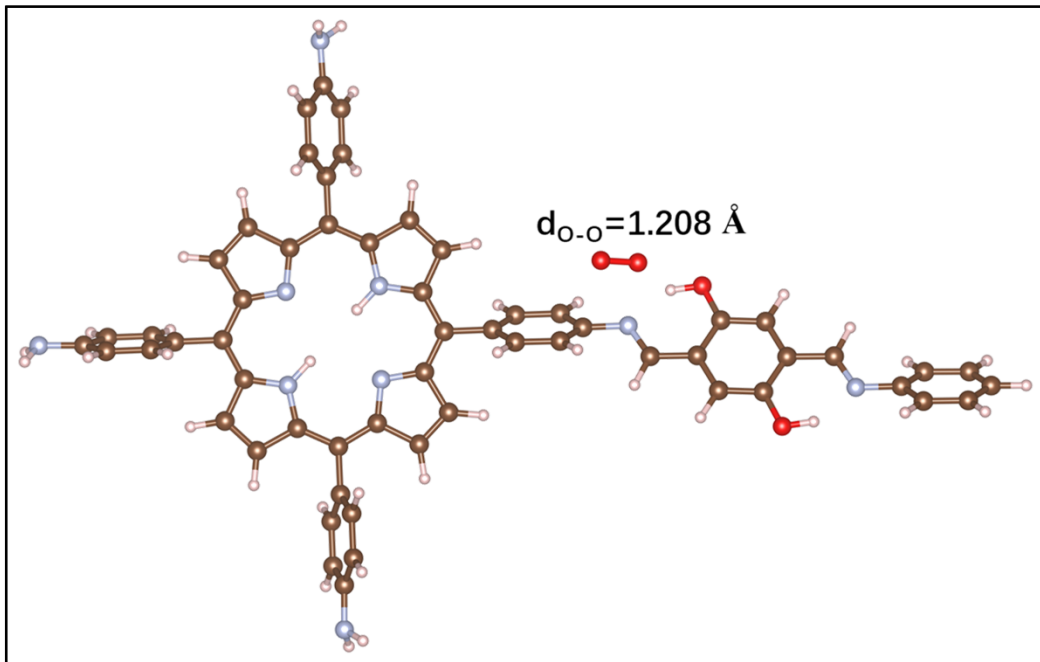


Figure S36. The optimized structure of O_2 adsorption on the Dha-TAPP.

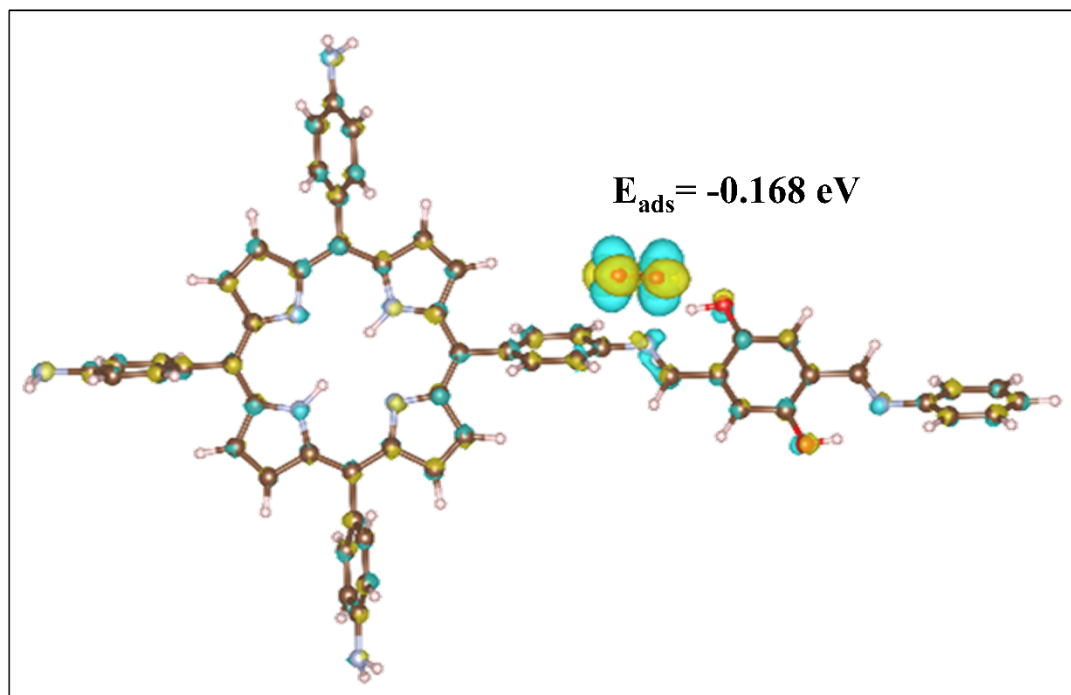


Figure S37. The charge density difference on the Dha-TAPP, in which the yellow and cyan are charge density concentration and depletion whose isovalue is 0.001 a.u. The yellow regions represent electron-rich areas, while the cyan areas are electron-deficient.

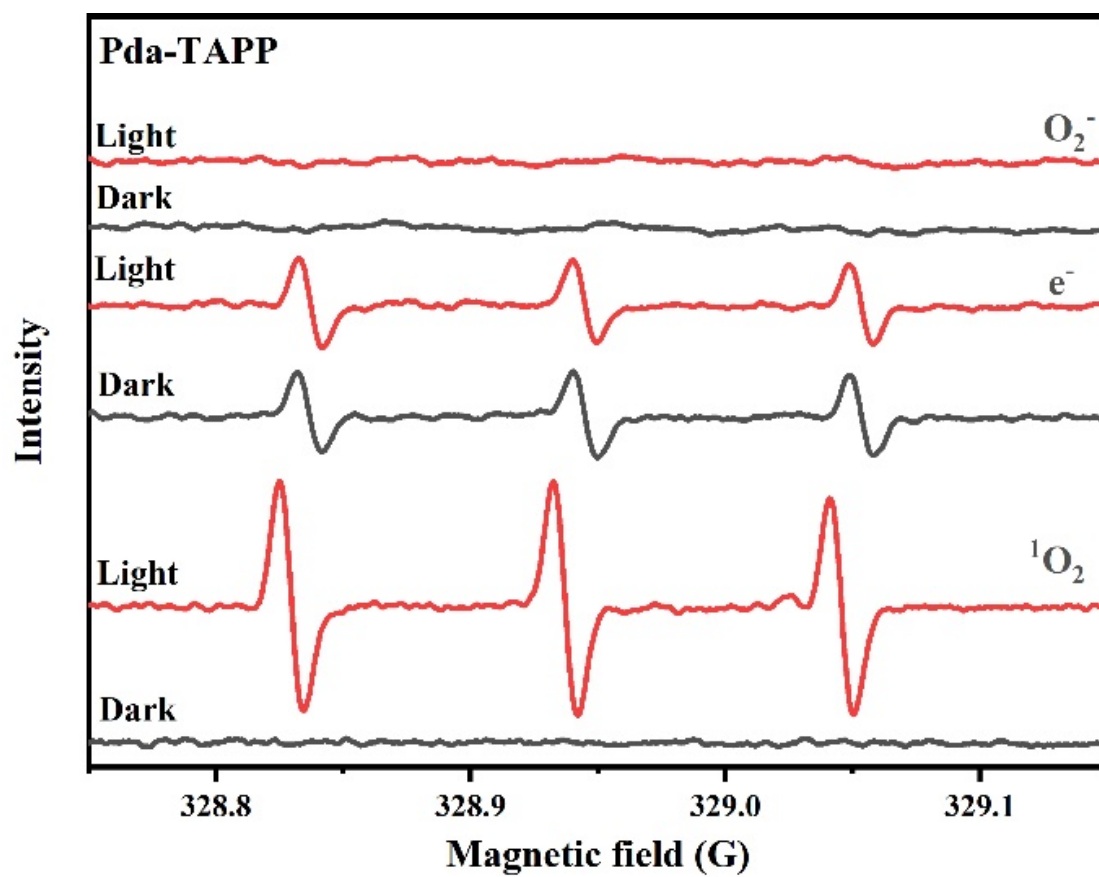


Figure S38. EPR spectra of $\cdot\text{O}_2^-$, e^- and $^1\text{O}_2$ over Pda-TAPP.

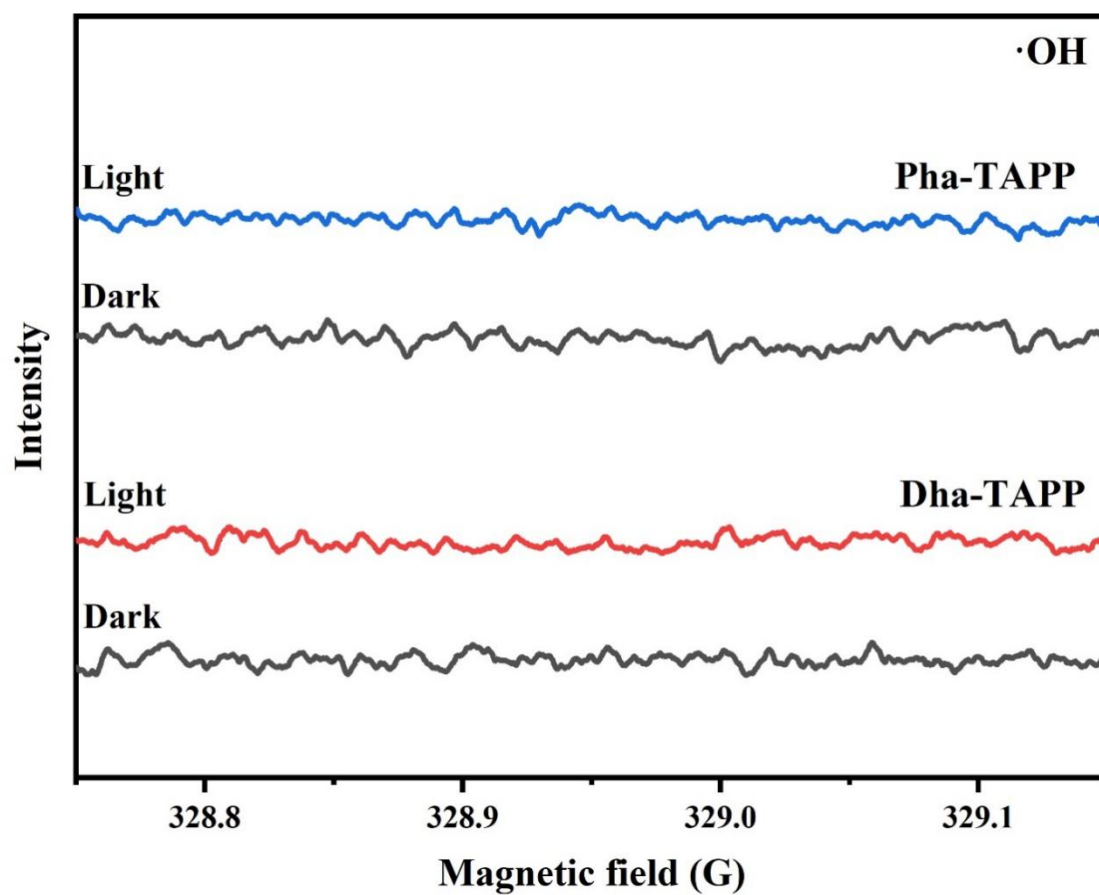


Figure S39. EPR spectra of $\cdot\text{OH}$ over Pda-TAPP and Dha-TAPP.

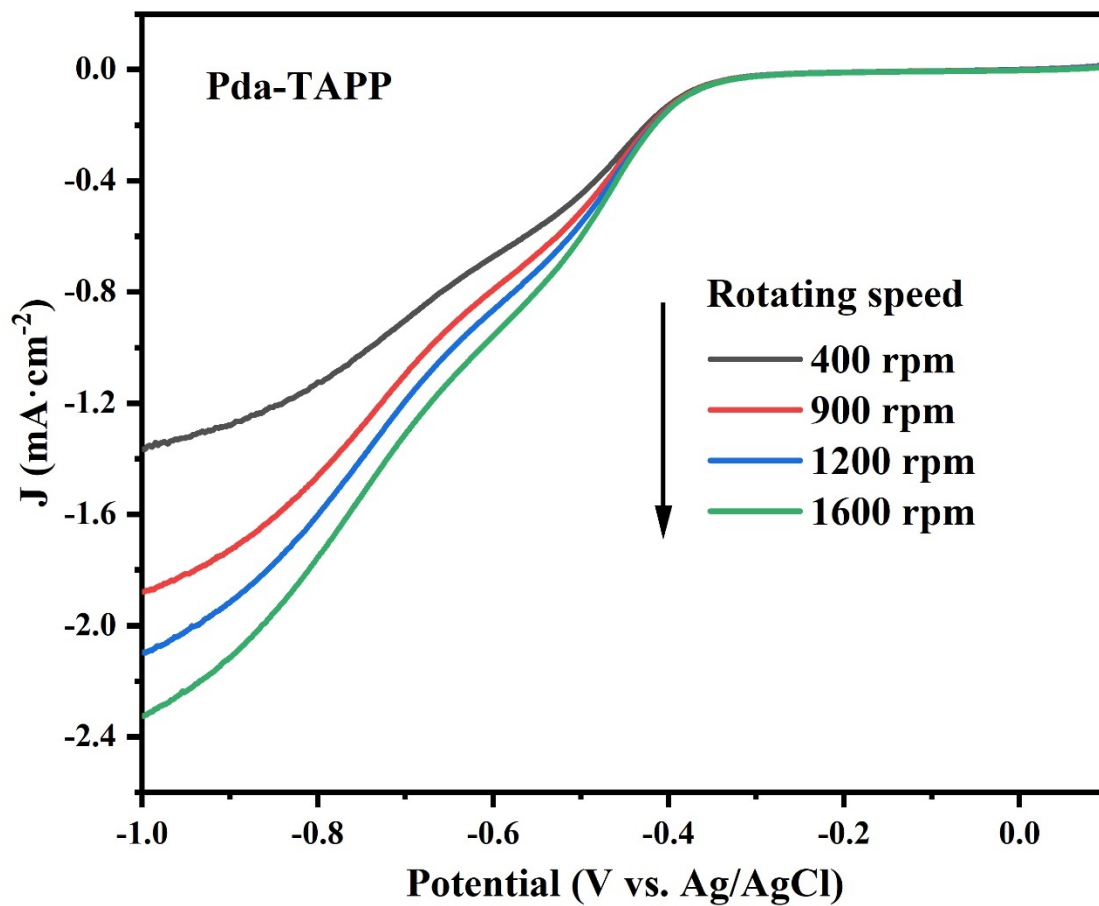


Figure S40. LSV curves of Pda-TAPP measured on RDE analysis at different rotating speeds.

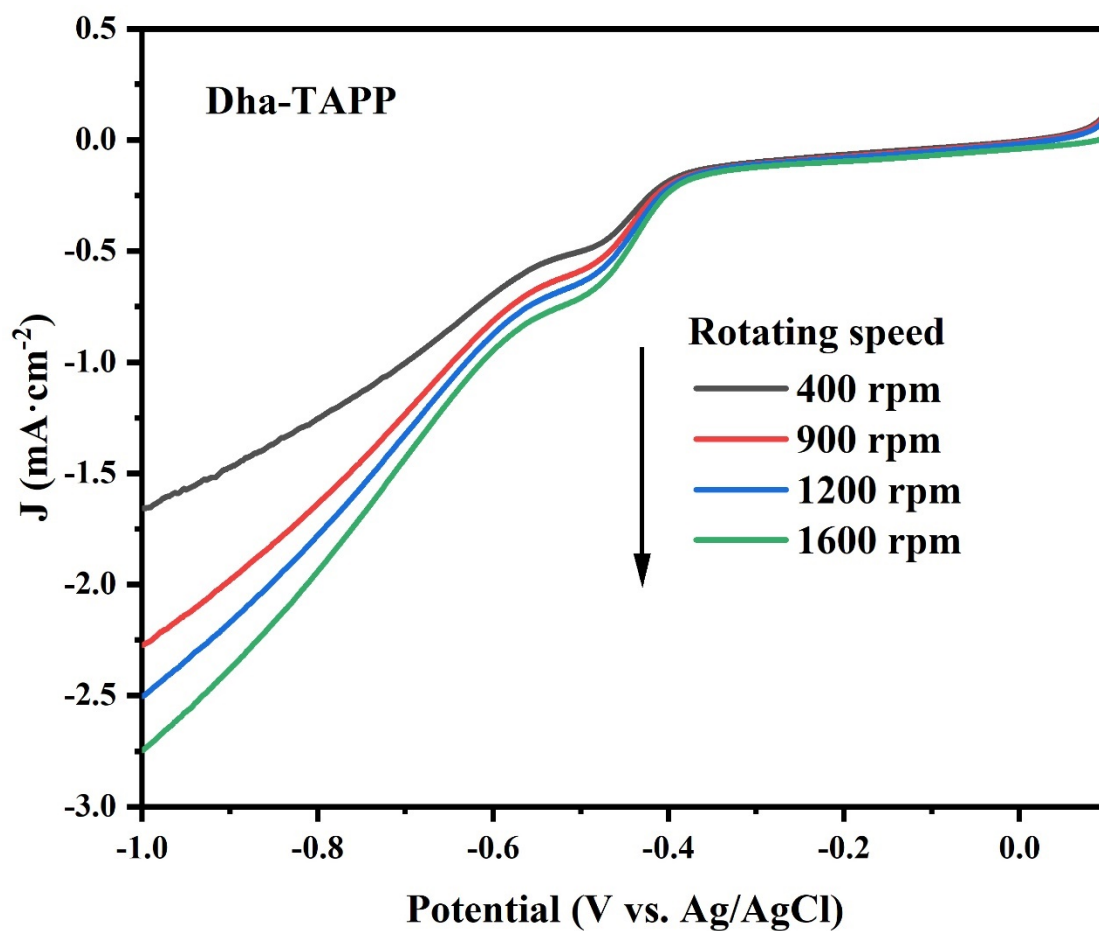


Figure S41. LSV curves of Dha-TAPP measured on RDE analysis at different rotating speeds.

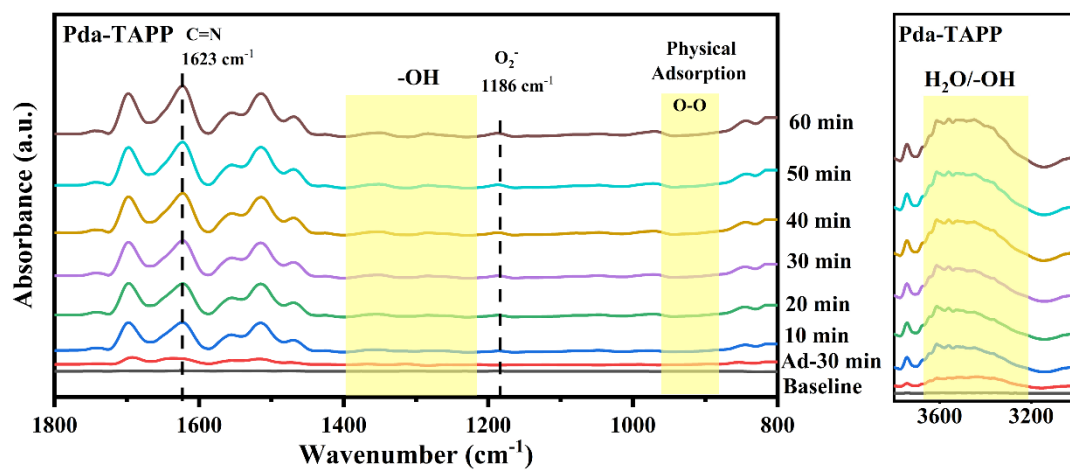


Figure S42. In-situ FT-IR spectrum of Pda-TAPP for photosynthetic H_2O_2 production at 800 cm^{-1} to 1800 cm^{-1} and 3000 cm^{-1} to 3800 cm^{-1} .

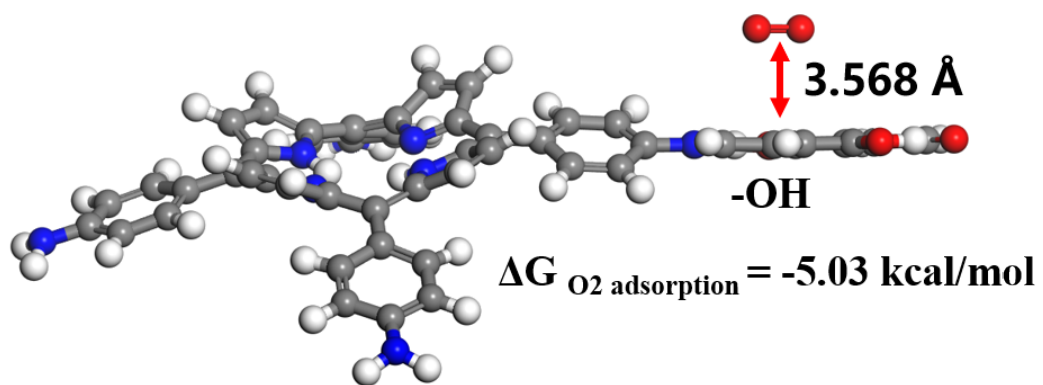


Figure S43. Calculated oxygen adsorption energies on the -OH of Dha-TAPP (C: gray; N: blue; O: red; H: white).

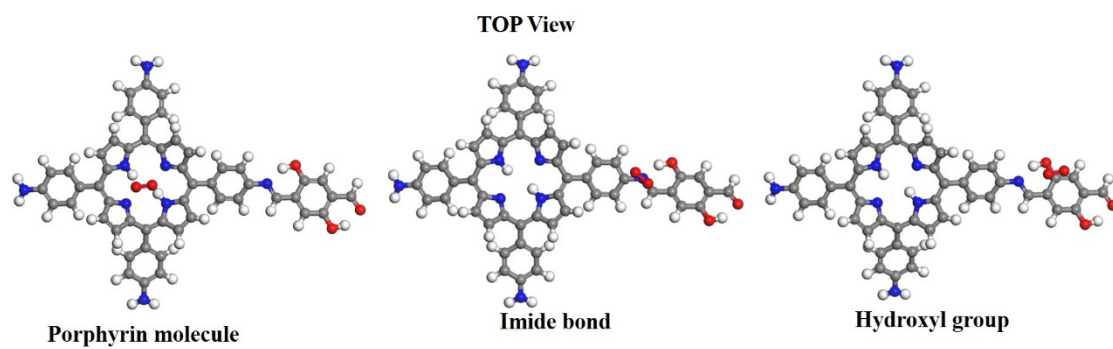
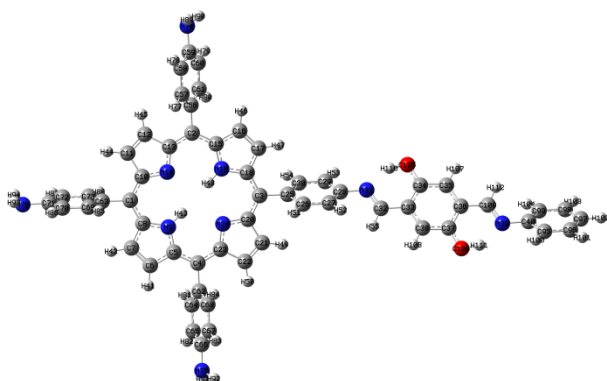


Figure S44. TOP view of calculated oxygen adsorption energies on Dha-TAPP (C: gray; N: blue; O: red; H: white).

S3. Supplementary Tables

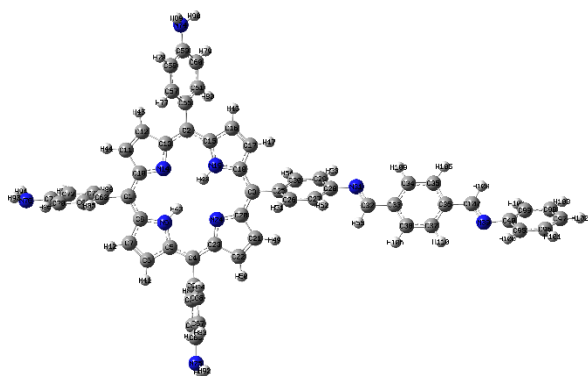
Table S1. The Hirshfeld atomic charges of Pda-TAPP and Dha-TAPP.

Molecule	Atom	Number	Charge
	C	1	-0.0059
	C	2	-0.0043
	C	3	-0.0094
	C	4	-0.0069
	C	5	0.0432
	C	6	-0.0565
	C	7	-0.0560
	C	8	0.0423
	N	9	-0.0450
	C	10	0.0266
	C	11	-0.0664
	C	12	-0.0655
	C	13	0.0257
	N	14	-0.1994
	C	15	0.0411
	C	16	-0.0581
	C	17	-0.0606
	C	18	0.0411
	N	19	-0.0440
	C	20	0.0251
	C	21	-0.0685
	C	22	-0.0657
	C	23	0.0267
	N	24	-0.2004
	C	25	0.0041
	C	26	-0.0362
	C	27	-0.0535
	C	28	0.0340
	C	29	-0.0486
	C	30	-0.0362
	N	31	-0.1106
	C	32	0.0660
	C	33	-0.0302
	C	34	0.0786
	C	35	-0.0566
	C	36	-0.0305
	C	37	0.0787
	C	38	-0.0565
	N	39	-0.1114
	C	40	0.0356
	H	41	0.0525



H	42	0.0531
H	43	0.1105
H	44	0.0452
H	45	0.0458
H	46	0.0513
H	47	0.0506
H	48	0.1110
H	49	0.0432
H	50	0.0455
H	51	0.0500
H	52	0.0449
H	53	0.0496
H	54	0.0492
H	55	0.0485
C	56	-0.0156
C	57	-0.0375
C	58	-0.0712
C	59	0.0468
C	60	-0.0722
C	61	-0.0388
C	62	-0.0157
C	63	-0.0152
C	64	-0.0390
C	65	-0.0719
C	66	0.0466
C	67	-0.0715
C	68	-0.0383
C	69	-0.0393
C	70	-0.0718
C	71	0.0462
C	72	-0.0714
C	73	-0.0387
N	74	-0.1856
N	75	-0.1859
N	76	-0.1865
H	77	0.0474
H	78	0.0408
H	79	0.0405
H	80	0.0460
H	81	0.0465
H	82	0.0406
H	83	0.0407
H	84	0.0470
H	85	0.0468

	H	86	0.0405
	H	87	0.0406
	H	88	0.0474
	H	89	0.1209
	H	90	0.1207
	H	91	0.1207
	H	92	0.1206
	H	93	0.1204
	H	94	0.1205
	C	95	-0.0483
	C	96	-0.0395
	C	97	-0.0456
	C	98	-0.0409
	C	99	-0.0536
	H	100	0.0489
	H	101	0.0490
	H	102	0.0474
	H	103	0.0485
	H	104	0.0441
	O	105	-0.2123
	O	106	-0.2119
	H	107	0.0507
	H	108	0.0508
	C	109	0.0660
	H	110	0.1196
	H	111	0.1201
	H	112	0.0482
	C	1	-0.0076
	C	2	-0.0040
	C	3	-0.0069
	C	4	-0.0082
	C	5	0.0432
	C	6	-0.0563
	C	7	-0.0560
	C	8	0.0427
	N	9	-0.0457
	C	10	0.0272
	C	11	-0.0670
	C	12	-0.0654
	C	13	0.0249
	N	14	-0.1997
	C	15	0.0407
	C	16	-0.0593
	C	17	-0.0604



C	18	0.0407
N	19	-0.0436
C	20	0.0245
C	21	-0.0678
C	22	-0.0668
C	23	0.0270
N	24	-0.2004
C	25	0.0008
C	26	-0.0382
C	27	-0.0560
C	28	0.0351
C	29	-0.0499
C	30	-0.0382
N	31	-0.1398
C	32	0.0558
C	33	-0.0076
C	34	-0.0308
C	35	-0.0364
C	36	-0.0076
C	37	-0.0307
C	38	-0.0362
N	39	-0.1397
C	40	0.0359
H	41	0.0524
H	42	0.0530
H	43	0.1104
H	44	0.0449
H	45	0.0457
H	46	0.0507
H	47	0.0509
H	48	0.1110
H	49	0.0435
H	50	0.0450
H	51	0.0485
H	52	0.0428
H	53	0.0482
H	54	0.0476
H	55	0.0399
C	56	-0.0152
C	57	-0.0374
C	58	-0.0714
C	59	0.0466
C	60	-0.0722
C	61	-0.0387

C	62	-0.0154
C	63	-0.0151
C	64	-0.0391
C	65	-0.0721
C	66	0.0462
C	67	-0.0716
C	68	-0.0383
C	69	-0.0394
C	70	-0.0720
C	71	0.0460
C	72	-0.0715
C	73	-0.0388
N	74	-0.1859
N	75	-0.1863
N	76	-0.1868
H	77	0.0474
H	78	0.0407
H	79	0.0404
H	80	0.0461
H	81	0.0465
H	82	0.0404
H	83	0.0405
H	84	0.0470
H	85	0.0467
H	86	0.0404
H	87	0.0405
H	88	0.0473
H	89	0.1207
H	90	0.1205
H	91	0.1205
H	92	0.1204
H	93	0.1203
H	94	0.1203
C	95	-0.0499
C	96	-0.0420
C	97	-0.0495
C	98	-0.0435
C	99	-0.0564
H	100	0.0473
H	101	0.0471
H	102	0.0454
H	103	0.0466
H	104	0.0418
H	105	0.0474

H	106	0.0476
C	107	0.0555
H	108	0.0397
H	109	0.0491
H	110	0.0492

Table S2 Comparison of recent photocatalytic performance of H₂O₂ produced by other photocatalytic materials

Samples	solution	atmosphere	Light condition	H ₂ O ₂ ($\mu\text{mol}\cdot\text{g}^{-1}\cdot\text{h}^{-1}$)	Ref.
ANQ-POP	H ₂ O	O ₂	$\lambda > 400$ nm	160	1
COF-NUST-16	H ₂ O	O ₂	$\lambda \geq 400$ nm	223.55	2
TTF-BT-COF	H ₂ O	O ₂	$\lambda > 420$ nm	2760	3
HEP-TAPT-CO F	H ₂ O	O ₂	$\lambda > 420$ nm	1750	4
TF ₅₀ -COF	10% EtOH	O ₂	$\lambda > 400$ nm	1739	5
NMT-400	10% EtOH	Air	AM 1.5G	270.9	6
Py-Da-COF	10% BA	O ₂	$\lambda > 420$ nm	1242	7
TAPD-(OMe) ₂ COF	10% EtOH	O ₂	$420 < \lambda < 700$ nm	97	8
sonoCOF-F2	H ₂ O	Air	AM 1.5G	1244.44	9
CoPc-BTM-CO F	10% EtOH	O ₂	$\lambda > 400$ nm	2096	10
DMCR-1NH	H ₂ O	Air	$\lambda > 420$ nm	2264.5	11
Pda-TAPP	H₂O	Air	AM 1.5G	675.6	This work
Dha-TAPP	H₂O	Air	AM 1.5G	2905.1	This work
Dha-TAPP	3 mM ASA	Air	AM 1.5G	9689.0	This work

Table. S3 The Fukui index of CIP

atom	f(-)	f(+)	f(0)
O (1)	0.038	0.048	0.043
C (2)	0.006	0.011	0.008
C (3)	0.016	0.013	0.015
C (4)	0.021	0.092	0.056
N (5)	0.01	0.011	0.011
C (6)	-0.024	-0.035	-0.029
C (7)	-0.005	-0.002	-0.004
C (8)	0.004	-0.002	0.001
C (9)	0.02	0.013	0.017
C (10)	0.027	-0.006	0.01
C (11)	0.014	0.063	0.039
C (12)	0.028	0.032	0.03
F (13)	0.027	0.037	0.032
C (14)	0.006	0.045	0.025
N (15)	0.049	0.019	0.034
C (16)	-0.025	-0.025	-0.025
C (17)	-0.02	-0.007	-0.014
N (18)	0.084	0.015	0.049
C (19)	-0.02	-0.008	-0.014
C (20)	-0.03	-0.025	-0.027
C (21)	0.025	0.049	0.037
C (22)	0.023	0.064	0.043
O (23)	0.125	0.099	0.112
O (24)	0.028	0.033	0.031
H (25)	0.037	0.055	0.046
H (26)	0.021	0.041	0.031
H (27)	0.006	0.012	0.009

H (28)	0.017	0.032	0.024
H (29)	0.013	0.014	0.014
H (30)	0.026	0.035	0.03
H (31)	0.035	0.046	0.041
H (32)	0.033	0.011	0.022
H (33)	0.052	0.032	0.042
H (34)	0.038	0.014	0.026
H (35)	0.048	0.027	0.038
H (36)	0.037	0.012	0.024
H (37)	0.039	0.016	0.027
H (38)	0.048	0.027	0.037
H (39)	0.035	0.01	0.023
H (40)	0.052	0.027	0.04
H (41)	0.026	0.04	0.033
H (42)	0.01	0.014	0.012

S4. Supplementary References

1. W. Chongbei, T. Zhenyuan, Y. Chao, C. Fangshuai, Y. H. Bin, W. Lei, X. Hangxun, L. Bin, Z. Gengfeng and H. Qing, *Advanced materials (Deerfield Beach, Fla.)*, 2022, 34, e2110266-e2110266.
2. B. Bishal, K. Nayeong, K. Jae-Seung, P. Ratul, N. Yogendra, C. Yuri, S. Dong-Hwa, M. John and R. Jungki, *Journal of Colloid And Interface Science*, 2023, 652, 1784-1792.
3. C. JiaNan, L. Qi, S. JingWen, Z. Mi, Z. Lei, L. Shan, C. Yifa, L. ShunLi and L. YaQian, *Angewandte Chemie*, 2023, 135.
4. C. Dan, C. Weiben, W. Yuting, W. Lei, W. Xiaojun, X. Hangxun and C. Long, *Angewandte Chemie*, 2023, 135.
5. W. Haozhen, Y. Chao, C. Fangshuai, Z. Gengfeng and H. Qing, *Angewandte Chemie*, 2022, 134.
6. C. Yang, S. J. Wan, B. C. Zhu, J. G. Yu and S. W. Cao, *Angewandte Chemie-International Edition*, 2022, 61.
7. J. Sun, H. S. Jena, C. Krishnaraj, K. S. Rawat, S. Abednatanzi, J. Chakraborty, A. Laemont, W. Liu, H. Chen, Y. Liu, K. Leus, H. Vrielinck, V. V. Speybroeck and P. V. D. Voort, *Angewandte Chemie International Edition*, 2023, 62.
8. K. Chidharth, S. J. Himanshu, B. Laurens, L. Andreas, P. Pradip, R. Jérôme, C. C. Vinod, B. Sander, R. S. M. J, L. Karen, S. C. V, M. J. A, V. S. Veronique, B. Eric, T. Arne and V. D. V. Pascal, *Journal of the American Chemical Society*, 2020, 142, 20107-20116.
9. Z. Wei, Y. Peiyao, L. Boyu, B. Mounib, L. Lunjie, Z. Xiang, C. Rob, B. N. D, W. Yue, W. J. W and C. A. I, *Journal of the American Chemical Society*, 2022, 144.
10. Z. Qianjun, L. Wenping, J. Rong, Z. Xiaoning, J. Yucheng, C. Xin, Y. Xiya, W. Kang, C. Wei, Q. Dongdong and J. Jianzhuang, *Journal of the American Chemical Society*, 2022, 144.
11. D. Prasenjit, C. Gouri, R. Jérôme, V. Sarah, R. Jabor and T. Arne, *Journal of the American Chemical Society*, 2023, 145